NANOMECHANICAL RESPONSES OF BORON CARBIDE

A Thesis

by

HSU-MING LIEN

Submitted to the Office of Graduate and Professional Studies of
Texas A&M University
in partial fulfillment of the requirements for the degree of

MASTER OF SCIENCE

Chair of Committee,	Kelvin Y. Xie
Committee Members,	Mohammad Naraghi
	Pavan V. Kolluru
Head of Department,	Ibrahim Karaman

August 2020

Major Subject: Materials Science and Engineering

ABSTRACT

Nanomechanical responses of brittle materials, such as glass and ceramics, are important for various industrial applications. Understanding their deformation and failure mechanisms would offer new knowledge and help design materials with better performance. Among brittle materials, boron carbide is of interest due to its low density, high hardness, and chemical inertness. However, the nanomechanical responses of boron carbide are less known compared to other brittle materials. In this work, we performed nanoindentation at various loads with a Berkovich indenter on the undoped, B-doped, and B/Si co-doped boron carbide samples to investigate their nanomechanical responses. Pop-in events were observed in the load-displacement curves for all samples. The loads to trigger the first pop-in in the B-doped boron carbide are rather scattered. In contrast, consistent distributions of the first pop-ins, which corresponds to the onset of plasticity, were noted in the undoped and B/Si co-doped boron carbide. With that, the power-law fitting and the standard Hertzian contact fitting were applied for these materials to derive the maximum shear stress induced by nanoindentation, with 25.94 ± 0.57 GPa for the undoped boron carbide and 24.47 ± 0.52 GPa for the B/Si co-doped boron carbide. Besides, cracking (both the surface and subsurface ones) was also induced by nanoindentation. The surface cracks were studied through scanning electron microscopy. Surface crack lengths were measured and then applied to estimate the indentation fracture toughness through the model assuming half-penny cracks. The estimated indentation fracture toughness values for undoped, B-doped, and B/Si co-doped boron carbide are 3.15 ± 0.65 MPa $m^{1/2}$,4.91 ± 0.66 MPa $m^{1/2}$, and 2.79 ± 0.39 MPa $m^{1/2}$, respectively. To verify the assumption, serial focused ion beam cross-sectioning was employed to reveal the subsurface

cracks beneath the 500mN-load indentation impressions. The results suggested the model overlooked the contribution from edge cracks and lateral cracks. To sum up, from the nanomechanical responses, we revealed that *1)* the maximum shear stress required to trigger the first pop-in event is higher in the undoped boron carbide, and *2)* the B-doped boron carbide displays the highest indentation fracture toughness although the true value is underestimated. This work also illuminated how the dopants influence the deformation behavior behind the physical phenomena.

DEDICATION

Dedicated to my mom, Shu-ling, my dad, Shan-Yao, and my sisters, Li-Yi and Li-Wei. Despite the hardship happened to you all in 2019, still believe in me and support my studies and dreams.

ACKNOWLEDGEMENTS

I would like to thank my committee chair, Dr. Xie, and committee members, Dr. Naraghi and Dr. Kolluru, for their guidance and support throughout the course of this research.

In addition, I am very thankful for all of the mentors I have been fortunate to surround myself with at Texas A&M University. Especially thank you to former post-docs in our group, Dr. Xiang and Dr. Ma, for leading me into the field of research and sharing your experiences of pursuing greatness.

Thanks also go to my colleagues and friends and department faculty and staff for making my time at Texas A&M University a great experience.

Lastly, thanks to my parents and my sisters for their continuing supports, both financially and mentally, to my pursuit of graduate degree in the US, despite the great hardship they have experienced throughout the past several months.

CONTRIBUTORS AND FUNDING SOURCES

Contributors

This work was supervised by a thesis committee consisting of Professor Xie and Professor Kolluru of the Department of Materials Science and Engineering and Professor Naraghi of the Department of Aerospace Engineering.

The samples used in this research were provided by the collaborators at Rutgers University. Professor Rich Habor and his student, Bruce Yang, fabricated the samples with the funds from Army Research Lab.

Nanoindentation was conducted by Professor Pharr and his student, Yvonne Dieudonne from the Department of Materials Science and Engineering.

All other works conducted for the thesis was completed by the student independently.

Funding Sources

Graduate study was supported by the MSEN scholarship from the Department of Materials Science and Engineering at Texas A&M University.

This work was made possible through the Army Research Laboratory under the Cooperative Agreement number W911NF-12-2-0022, the Defense Advanced Research Project Agency under the grant number W31P4Q-13-1-000, and Professor Xie's start-up funding from the Department of Materials Science and Engineering at Texas A&M University. Its contents are solely the responsibility of the authors and do not necessarily represent the official views of the Department of Materials Science and Engineering.

TABLE OF CONTENTS

Page

LIST OF FIGURES

Page

LIST OF TABLES

Page

1. INTRODUCTION

Brittle materials, such as ceramics and glass, have drawn a substantial attention because of their outstanding properties that are rarely observed in metals and polymers. For example, boron carbide has been applied for various industrial applications, such as blasting nozzles and body armor, due to its low density, high hardness, and chemical inertness [1-3]. Boron carbide also exhibits high neutron absorption cross-section, thus being used in nuclear industries [2, 4]. These macroscopic performances are associated with the nanomechanical responses in material, and hence, understanding the deformation and failure mechanisms behind the observed phenomena would offer new knowledge and help design materials with better performance. Up to date, despite of various applications being developed for boron carbide, the deformation mechanisms upon impact of this material are less known, compared with other brittle materials [5, 6]. For instance, dislocation nucleation [7] and deformation twin [8] had been observed in sapphire as the responses to the onset of plasticity, and these findings were later applied for improving the micro-machining parameters. Therefore, there is a need to fully understand the underlying mechanism of nanomechanical responses in boron carbide to improve its impact performance. More specifically, this work aims to investigate the effect on dopant on the deformation and fracture behavior of boron carbide using nanoindentation as a testing tool.

1.1 References

1. Vladislav Domnich, S.R., Richard A. Haber, Manish Chhowalla, *Boron Carbide: Structure, Properties, and Stability under Stress.* Journal of American Ceramic Society, 2011. **94**: p. 3605-3628.

2. Thévenot, F., *Boron Carbide A Comprehensive Review.* Journal of the European Ceramic Society, 1990. **6**(4): p. 205-225.

3. A. K. Suri, C.S., J. K. Sonber, T. S. R. Ch. Murthy, *Synthesis and consolidation of boron carbide: a review.* International Materials Reviews 2010. **55**(1): p. 4-40.

4. David Emin, T.L.A., *A proposed boron-carbide-based solid-state neutron detector.* Journal of Applied Physics, 2005. **97**.

5. T. F. Page, L.R., S.V. Hainsworth, The Plasticity Response Of 6H-SiC and Related Isostructural Materials to Nanoindentation: Slip vs Densification. MRS Proceedings, 1998. **522**.

6. Jae-il Jang and S.W. M. J. Lance, Ting Y. Tsui, G. M. Pharr Indentation-induced phase transformations in silicon: influences of load, rate and indenter angle on the transformation behavior. Acta Materialia, 2005. **53**: p. 1759–1770.

7. Trevor F. Page, W.C.O., Carl J. McHargue, *The deformation behavior of ceramic crystals subjected to very low load (nano)indentations.* Journal of Materials Research, 1992. **7**(2): p. 450-473.

8. V. Trabadelo, S.P., F. Saeidi, M. Parlinska-Wojtan, K. Wasmer, *Nanoindentation deformation and cracking in sapphire.* Ceramics International, 2019. **45**: p. 9835–9845.

2. LITERATURE REVIEW

2.1 Crystal Structure and Mechanical Properties of Boron Carbide

The typical crystal structure of boron carbide is composed of 12-atom icosahedra and 3-atom chains. Several theoretical simulations have been proposed to predict the most probable configuration for boron carbide. So far, there are B_{12}, $B_{11}C$, $B_{10}C_2$, and B_9C_3 reported for icosahedral configuration and CCC, CBC, CCB, CBB, BCB, and BBB for the chain [1-4]. Also, nonlinear chains composed of 4 boron atoms and chains with vacancies were suggested in these studies. Among these polymorphs, ($B_{11}C$) CBC, with the icosahedral C placing at the polar site, has been proved energetically favorable for the theoretical calculation.[5-7] From the experimental viewpoint, Raman spectroscopy [8-11] and X-ray diffraction [12, 13] have also implied the configuration of ($B_{11}C^p$) CBC, with the letter "p" signifying the icosahedral polar site. Therefore, the majority of theoretical and experimental investigations have arrived to a consensus that ($B_{11}C^p$) CBC is the preferred configuration for boron carbide.

Like other carbides, boron carbide demonstrates extremely high elastic modulus as well as hardness, which ranks only behind diamond and cubic boron nitride among known materials [4, 14]. The reported elastic modulus is approximately 500 GPa [4, 15]. Unlike elastic modulus is an intrinsic material property, hardness depends on various external factors, for example grain size, defects, and porosity. Nevertheless, the typical hardness values of boron carbide are reported in the range between 20 and 28 GPa for Vickers indentation [13, 15], 29 and 31 GPa for Knoop indentation [14], and 41 and 50 GPa for nanoindentation [13, 15].

With the outstanding mechanical properties, boron carbide was proposed for body armor applications, but the results of ballistic impact suggested that the performance fell far behind

than expected. Chen and co-authors had reported localized phase transformation in boron carbide from the TEM analysis of the post-impact fragmentation and later attributed that to the reason for the decrease in ballistic performance [16]. From then on, several methods have been proposed to mitigate the amorphization in boron carbide, and among those, doping is considered the most effective [17-19]. So far, Si doping has been widely reported for the effect of stabilizing the crystal structure of boron carbide. Khan *et al.* reported both theoretical and experimental results that replacing the chain-center boron with Si atom could stabilize the crystal structure by forming an additional bond with the neighboring icosahedral boron [20]. Subsequently, Xiang *et al.* have further suggested that Si-doping could change the deformation mechanism in boron carbide from amorphization to direct fragmentation via TEM-based analyses [21]. However, it has also been argued that the reduced amount of strong covalent bond, for example B-C bonds, in boron carbide would result in lower hardness and elastic modulus [15]. Indeed, the reported numbers for undoped boron carbide are generally higher than that of doped boron carbide.

2.2 Mechanical Properties Measurement from Nanoindentation

Nanoindentation is widely known for its capability of deriving mechanical properties from a small volume of material, and therefore it has been applied to various fields of study [22-24]. The most commonly reported application is the acquisition of the hardness and elastic modulus of the probed material. Hardness is defined as the capability of resisting permanent deformation and can be expressed as the applied load divided by the projected contact area. However, it is difficult to directly and precisely measure the contact area due to the dimension of the nanoindentation impressions. Pethicai *et al.* first introduced the concept of area function to tackle this issue but did not provide further insight [25]. Subsequently, Doerner and Nix proposed a method to derive hardness and elastic modulus from the load-displacement curve by

assuming that the unloading portion followed the response of flat punch indenter [26]. However, in most of the cases, the unloading curve is not linear, thus rendering their analysis untenable.

Following their predecessors, Oliver and Pharr revisited the concept of area function and eventually came up with a method to acquire hardness and elastic modulus without imaging the imprints [27]. They started with the nonlinear response of unloading curve and suggested to adapt Sneddon's analysis of axisymmetric indenter tip [28] for describing the unloading behavior. Next, based on Sneddon's analysis, they established the relationship between contact stiffness and unloading curve. With that as the basis, they evaluated various materials and eventually suggested fused quartz as the standard material to calibrate the area function due to its well-studied mechanical properties. Once being calibrated, the contact area can be described as a function of contact depth, which is a measurable term in nanoindentation, and therefore hardness can be calculated from its definition. As for elastic modulus, it can be derived as following [29]:

$$\frac{1}{E_r} = \frac{1-\nu_i{}^2}{E_i} + \frac{1-\nu_s{}^2}{E_s} \qquad \text{(Eq. 2.1)}$$

where E and ν are the elastic modulus and Poisson's ratio, with the subscript "i" and "s" denoting the diamond indenter and the sample, and E_r is the reduced modulus proposed by Hertz to account for the elastic deformation of the indenter tip. To obtain E_r, one has to apply the essential equation of nanoindentation [30]:

$$E_r = \frac{\sqrt{\pi}}{2}\frac{S}{\sqrt{A}} \qquad \text{(Eq. 2.2)}$$

where S is the contact stiffness and A is the calibrated contact area in terms of contact depth. For these two terms are measurable, E_r can be derived and the elastic modulus of the sample can be computed through Eq. 2.1.

2.3 Indentation-induced Surface and Subsurface Cracking

Both micro-indentation and nanoindentation have long been applied for studying the cracking behavior in brittle materials. Cook and Pharr had classified the cracking systems observed in Vickers indentation on various brittle materials [31]. For pyramidal indenter, for example Vickers and Berkovich, radial-median cracking system, or half-penny system, is more likely to form in brittle materials. However, there are outliers, for example soda-lime glass developing cone cracks upon Vickers indentation. A cracking system that was not covered in Cook and Pharr's work is edge cracking, which has been studied systematically on various glasses by Yoshida and co-authors [32, 33]. They suggested that for nanoindentation with Berkovich indenter tip, this type of cracking is initiated by the tensile stress induced along the fringes of an impression by the sinking-in upon loading.

A majority of studies in the indentation induced cracking focuses on fracture toughness [34-36]. Among those models for estimating the resistance to indentation induced fracture, Lawn, Evans, and Marshall (LEM) had formulated the most reliable one, which was based on the assumption of half-penny cracking system developed upon Vickers indentation, and that can be expressed as following [37]:

$$K_c = \alpha \left(\frac{E}{H}\right)^{\frac{1}{2}} \frac{P}{c^{3/2}} \qquad \text{(Eq. 2.3)}$$

where α, E, H, P, and c are the empirical constant, elastic modulus, hardness, applied load, and the measured crack length, respectively. Anstis *et al.* had further determined the empirical constant, α, to be 0.016 by evaluating various brittle materials and suggested that the number was universal [38]. On the contrary, Jang and Pharr argued that α is associated with the intrinsic material property and the geometry of the indenter tip [39]. They started with the same

assumption in the LEM model and solved it with the Hill's expanding cavity solutions, and then formulated the following expression for α:

$$\alpha = \frac{0.0352}{1-\nu} \ (\cot\psi)^{\frac{2}{3}} \qquad \text{(Eq. 2.4)}$$

with ν being the Poisson's ratio of a material and ψ being the half-included angle of an indenter.

Despite the advantages brought by the aforementioned method, for example relatively simple sample preparation compared with the standard method stated by ASTM [40], the derived term can only be treated as indentation fracture toughness due to the incomparable stress states between these two tests. Also, the crack length measurement is extremely subjective, resulting in the variation in the reported numbers for the same material [41]. Apart from that, a number of studies have argued that the existing models do not account for the contributions other than the half-penny cracking system. For example, Cuadrado *et al.* conducted serial FIB cross-sectioning on the nanoindentation impressions in various materials [42]. They observed lateral cracks emanating from median crack in single crystal Si and (0001)6H-SiC, and hence argued the derived numbers were overestimated. Based on the observation, it was recommended to conduct serial FIB cross-sectioning to determine the cracking tomography before estimating the resistance of indentation cracking through the existing models.

2.4 References

1. D. R. Armstrong, J.B., P. G. Perkins, *The Nature of the Chemical Bonding in Boron Carbide. IV. Electronic Band Structure of Boron Carbide, B13C 2, and three Models of the Structure BnC 3.* Acta Crystallographica, 1983. **B39**: p. 324-329.

2. Nathalie Vast, J.S., Emmanuel Betranhandy, *Boron carbides from first principles.* Journal of Physics: Conference Series, 2009. **176**.

3. Giovanni Fanchini, J.W.M., Manish Chhowalla, *Behavior of Disordered Boron Carbide under Stress.* Physical Review Letters, 2006. **97**(3).

4. Vladislav Domnich, S.R., Richard A. Haber, Manish Chhowalla, *Boron Carbide: Structure, Properties, and Stability under Stress.* Journal of American Ceramic Society, 2011. **94**: p. 3605-3628.

5. Francesco Mauri, N.V., Chris J. Pickard, *Atomic Structure of Icosahedral B4C Boron Carbide from a First Principles Analysis of NMR Spectra.* Physical Review Letters, 2001. **87**(8).

6. N. Vast, J.M.B., S. Baroni, A. Dal Corso, *Atomic structure and vibrational properties of icosahedral α-boron and B4C boron carbide.* Computational Materials Science, 2000. **17**: p. 127-132.

7. R. Lazzari, N.V., J. M. Besson, S. Baroni, A. Dal Corso, *Atomic Structure and Vibrational Properties of Icosahedral B4C Boron Carbide.* Physical Review Letters, 1999. **83**(16).

8. H. Werheit, V.F., U. Schwarz, M. Armbr¨uster, A. Leithe-Jasper, T. Tanaka and S. O. Shalamberidze, *On surface Raman scattering and luminescence radiation in boron carbide.* Journal of Physics: Condensed Matter, 2010. **22**.

9. Cody Kunka, A.A., Ghatu Subhash, *Evaluating boron-carbide constituents with simulated Raman spectra*. Scripta Materialia, 2017. **138**: p. 32–34.

10. H. Werheit, U.K., H. W. Rotter, S. O. Shalamberidze, *Isotopic effects on the phonon modes in boron carbide.* Journal of Physics: Condensed Matter, 2010. **22**.

11. Helmut Werheit, M.H.M., Anwar Hushur, *Phonon peculiarities at the high-pressure phase transition of B4.3C boron carbide.* Solid State Sciences, 2019(97).

12. Terry L. Aselage, R.G.T., *lattice Constants of Boron Carbides.* Journal of American Ceramic Society, 1992. **75**(8): p. 2207-2212.

13. Chun Cheng, K.M.R., Akihiko Hirata, Takeshi Fujita, Mingwei Chen, *Structure and mechanical properties of boron-rich boron carbides.* Journal of the European Ceramic Society, 2017. **37**: p. 4514-4523.

14. Thévenot, F., *Boron Carbide A Comprehensive Review.* Journal of the European Ceramic Society, 1990. **6**(4): p. 205-225.

15. Kelvin Y. Xie, V.D., Lukasz Farbaniec, Bin Chen, Kanak Kuwelkar, Luoning Ma, James W. McCauley, Richard A. Haber, K.T. Ramesh, Mingwei Chen, Kevin J. Hemker, *Microstructural characterization of boron-rich boron carbide.* Acta Materialia, 2017. **136**: p. 202-214.

16. Mingwei Chen, J.W.M., Kevin J. Hemker, *Shock-Induced Localized Amorphization in Boron Carbide.* Science, 2003. **299**(5612): p. 1563-1566.

17. Bin Tang, Q.A., and William A. Goddard III, *Improved Ductility of Boron Carbide by Microalloying with Boron Suboxide.* The Journal of Physical Chemistry C, 2015. **119**(43): p. 24649-24656.

18. Ghatu Subhash, A.P.A., Cody Kunka, Phillip Jannotti, Matthew DeVries *In search of amorphization-resistant boron carbide.* Scripta Materialia, 2016. **123**: p. 158-162.

19. Yidi Shen, G.L., Qi An, *Enhanced fracture toughness of boron carbide from microalloying and nanotwinning.* Scripta Materialia, 2019. **162**: p. 306-310.

20. Atta U. Khan, A.M.E., Xiaokun Yang, Vladislav Domnich, Kelvin Y. Xie, Chawon Hwang, Kristopher D. Behler, Mingwei Chen, Qi An, Jerry C. LaSalvia, Kevin J. Hemker, William A. Goddard III, Richard A. Haber, *Locating Si atoms in Si-doped boron carbide: A route to understand amorphization mitigation mechanism.* Acta Materialia, 2018. **157**: p. 106-113.

21. Sisi Xiang, L.M., Bruce Yang, Yvonne Dieudonne, George M. Pharr, Jing Lu, Digvijay Yadav, Chawon Hwang, Jerry C. LaSalvia, Richard A. Haber, Kevin J. Hemker, Kelvin Y. Xie, *Tuning the Deformation Mechanisms of Boron Carbide via Silicon Doping.* Science Advances, 2019.

22. J. Malzbender, G.d.W., *The use of the indentation loading curve to detect fracture of coatings.* Surface and Coatings Technology, 2001. **137**(1): p. 72-76.

23. J.G. Swadener, E.P.G., G.M. Pharr, *The correlation of the indentation size effect measured with indenters of various shapes.* Journal of the Mechanics and Physics of Solids, 2002. **50**: p. 681–694.

24. Schiffmann, K.I., *Determination of fracture toughness of bulk materials and thin films by nanoindentation: comparison of different models.* Philosophical Magazine, 2011. **91**: p. 1163-1178.

25. J. B. Pethicai, R.H., W. C. Oliver, *Hardness measurement at penetration depths as small as 20 nm.* Philosophical Magazine A, 1983. **48**(4): p. 593-606

26. M. F. Doerner, W.D.N., *A method for interpreting the data from depth-sensing indentation instruments.* Journal of Materials Research, 1986. **1**(4): p. 601-609.

27. Warren C Oliver, G.M.P., *An improved technique for determining hardness and elastic modulus using load and displacement sensing indentation experiments.* Journal of materials research, 1992. **7**(6): p. 1564-1583.

28. Sneddon, I.N., *The relation between load and penetration in the axisymmetric boussinesq problem for a punch of arbitrary profile.* International Journal of Engineering Science, 1965. **3**(1): p. 47-57.

29. Johnson, J.L., *Contact Mechanics*. 1985: Cambridge University Press.

30. G. M. Pharr, W.C.O., F. R. Brotzen, *On the generality of the relationship among contact stiffness, contact area, and elastic modulus during indentation.* Journal of Materials Research, 1992. **7**(3).

31. Robert F. Cook, G.M.P., *Direct Observation and Analysis of Indentation Cracking in Glasses and Ceramics.* Journal of American Ceramic Society, 1990. **73**(4): p. 787-817.

32. Satoshi Yoshida, M.K., Akiko Yokota, Shohei Sasaki, Akihiro Yamada, Jun Matsuoka, Naohiro Soga, Charles R. Kurkjian, *Direct observation of indentation deformation and cracking of silicate glasses.* Journal of materials research, 2015. **30**: p. 2291-2299.

33. Satoshi Yoshida, J.M., Ken Wada, Takahiro Fujimura, Akihiro Yamada, Naohiro Soga, *Evaluation of Sinking-In and Cracking Behavior of Soda-Lime Glass under Varying Angle of Trigonal Pyramid Indenter*. Frontiers in Materials, 2016. **3**.

34. B. Lawn, R.W., *Indentation fracture: principles and applications.* Journal of Materials Science, 1975. **10**: p. 1049-1081.

35. Laugier, M.T., *Palmqvist indentation toughness in WC-Co composites.* Journal of Materials Science Letters, 1987. **6**(8): p. 897-900.

36. Warren, P.D., *Determining the fracture toughness of brittle materials by Hertzian indentation.* Journal of the European Ceramic Society, 1995. **15**(3): p. 201-207.

37. B. R. Lawn, A.G.E., D. B. Marshall, *Elastic/Plastic Indentation Damage in Ceramics: The Mediad/Radial Crack System.* Journal of the American Ceramic Society, 1980. **63**(9-10): p. 574-581.

38. G. R. Anstis, et al., *A Critical Evaluation of Indentation Techniques for Measuring Fracture Toughness: I, Direct Crack Measurements.* Journal of the American Ceramic Society, 1981. **64**(9): p. 533-538.

39. Jae-il Jang, G.M.P., *Influence of indenter angle on cracking in Si and Ge during nanoindentation.* Acta Materialia, 2008. **56**: p. 4458–4469.

40. *Standard Test Method for Measurement of Fracture Toughness*. 2020, ASTM International.

41. Quinn, G.D., *Fracture Toughness of Ceramics by the Vickers Indentation Crack Length Method: A Critical Review*, in *Mechanical Properties and Performance of Engineering Ceramics II: Ceramic Engineering and Science Proceedings*, A.W. Rajan Tandon, Edgar Lara-Curzio, Editor. 2006. p. 45-62.

42. N. Cuadrado, J.S., D. Casellas, M. Anglada, E. Jiménez-Piqué *Geometry of nanoindentation cube-corner cracks observed by FIB tomography: Implication for fracture resistance estimation.* Journal of the European Ceramic Society, 2015. **35**: p. 2949–2955.

3. EXPERIMENTAL DETAILS

3.1 Overview

The materials used in this work were kindly provided by our collaborators at Rutgers University. In the next section, the processing methods for each material as well as operation parameters will be addressed in detail and summarized in **Table 3.1**.

Figure 3.1 shows the flow of sample preparation and analysis after receiving the materials from the collaborators at Rutgers University. All the materials underwent the exactly same procedures and were analyzed systematically.

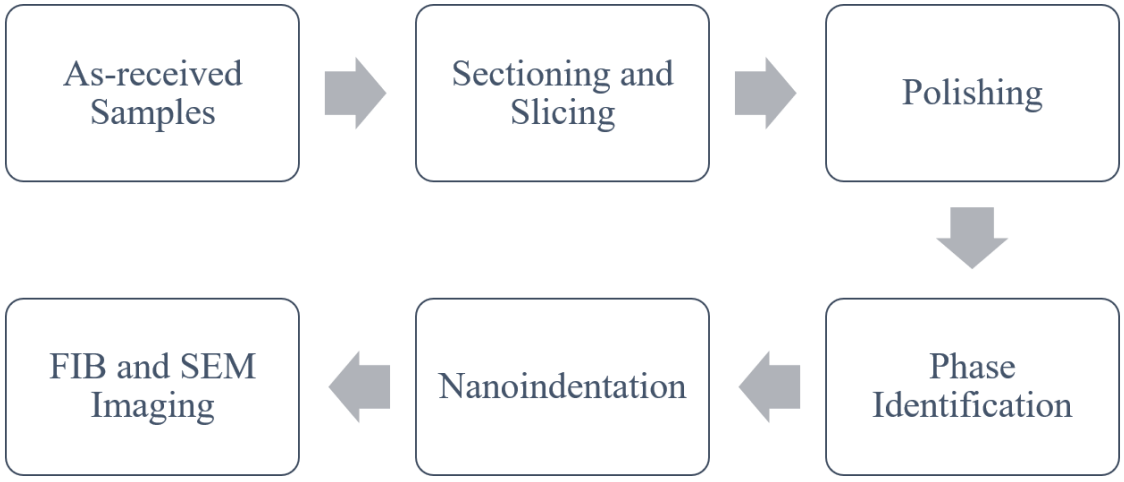

Figure 3.1 Schematic of the flow of the sample preparation for chemical and mechanical analysis.

Table 3.1 Summary of Sample Fabrication

Materials	Pure Boron Carbide	B-doped	B/Si co-doped
Nominal Composition	B_4C	$B_{13}C_2$	$B_{13}C_2$ + 1.5at% Si
Fabrication Method	Hot Press Sintering	Spark Plasma Sintering	Hot Press Sintering
Sintering Conditions	2150℃, 24 MPa, 4.5hr Ramp Rate: 12.5℃/s	1) 100℃/min. to 600℃ and hold for 1 min, 2) 300 ℃/min. to 1950℃ and hold for 5 min at 50 MPa	1950℃, 20 MPa, 3hr Ramp Rate: 12.8℃/s

3.2 Sample Fabrication and Phase Identification

Two processing methods were adopted for fabricating the materials used in this work. Regardless of the two different processing methods, the ultimate goal is to yield fully dense product and meanwhile ensure homogeneity in chemistry in each material. Hot-pressed sintering was selected for fabricating pure boron carbide (B_4C) and B/Si co-doped boron carbide, while spark plasma sintering (SPS) was chosen to fabricate B-doped boron carbide. The size of the as-received samples and the corresponding processing parameters, including sintering temperature and holding time, are summarized in the following table.

Before performing phase identification techniques on each material, all of them were sectioned and then sliced into appropriate sizes with low speed diamond saw. Due to the brittle nature of ceramics, all three samples were hot-mounted into transparent epoxy to prevent cracking into pieces during cutting. The solidified epoxy then served as the constraint to hold the material together as the low speed diamond was driven into the sample. Eventually, the three samples were cut into dimensions which are also listed in the following table.

After sectioning and slicing, the specimens were first mechanically polished with diamond lapping paper of 30 um and 15 um grades at 100 rpm and 80 rpm, respectively, to remove the apparent scratches on the surface. Later, they were further polished with 9um, 6um, and 1um water-based diamond suspension at 60 rpm on polishing pad to achieve mirror-like surface finish for phase identification.

Phase identification was carried out with X-ray diffractometer and Raman Spectrometer. X-ray diffraction (XRD) utilizes the interactions between the lattice atoms and the irradiated photons to characterize the identity of a material. **Figure 3.2** schematically shows how the Bragg diffraction takes place within atomic scales. Prior to irradiation, the sample stage was calibrated to be parallel with the surface of the sample in case of any artifact contributed by the surface tilting. The information acquired from this technique was further analyzed using Rietveld Refinement to simulate the phases presence in the probed specimen. The type of X-ray used in this experiment is Cu Kα, which has the wavelength of 1.54 Å, and meanwhile the scan speed was kept at 0.015°/s over the range from 15° to 90° in two-theta angle. The low scan speed could enhance the accuracy of the result of Rietveld Refinement because of the higher resolution in lattice information.

Raman Spectroscopy is a spectroscopic technique based on inelastic scattering of monochromatic electromagnetic wave, usually from a laser source. **Figure 3.3** illustrates how a photon interacts with a molecule and the corresponding change in energy. In this study, boron carbide exhibits the response to monochromatic light in the form of Stokes-Raman scattering, i.e. there is an energy loss in incident photons. By measuring the energy difference, the vibrational energy of the irradiated molecule could be deduced. Monochromatic red laser (633 nm) was selected in this work to excite certain vibrational modes in the samples. For each measurement,

the exposure time was held at 30 seconds per cycle, and in total there were three cycles in every measurement. The acquired data was normalized later to show the relative intensity and distribution of each Raman band.

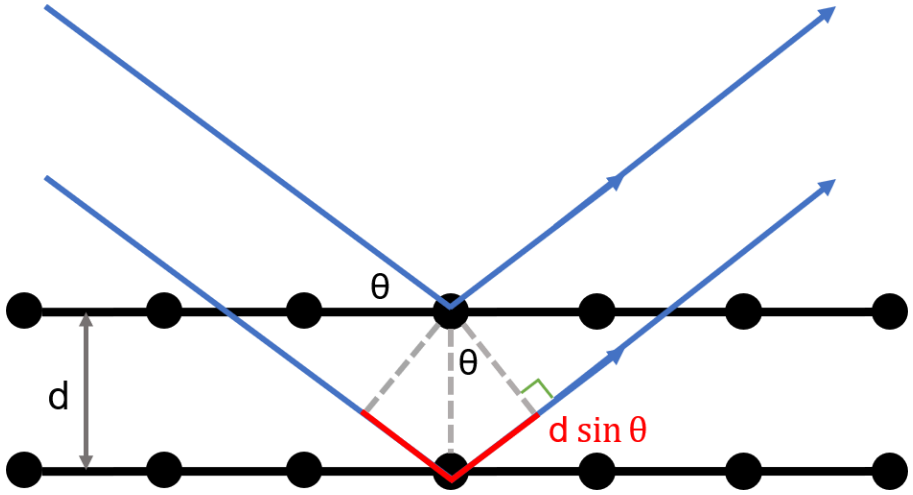

Figure 3.2 Schematic of Bragg's diffraction. The difference in the traveling distance between the incident and diffracted X-ray beam is defined as $2d\ sin\ \theta$.

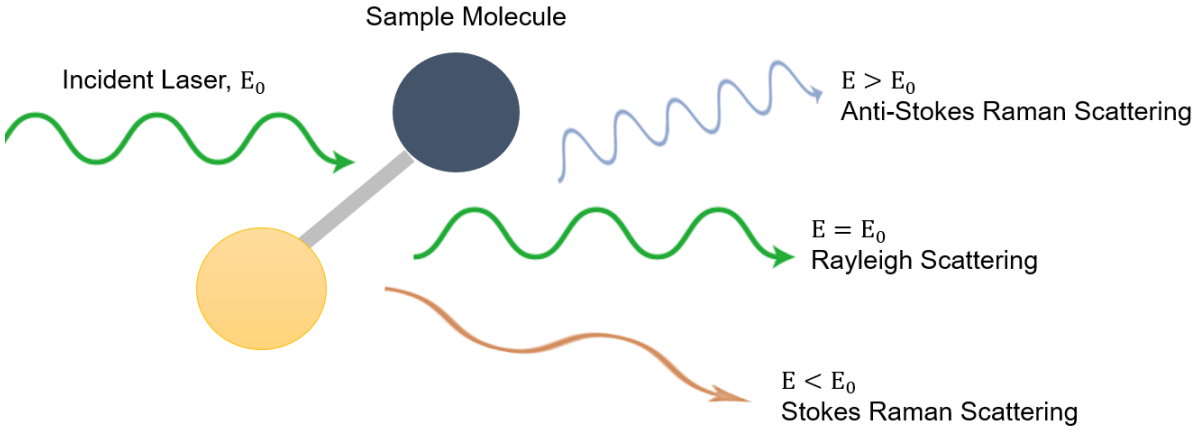

Figure 3.3 Schematic of the interaction between laser and irradiated sample molecule. Based on the energy of the scattered photon, it can be classified as Rayleigh Scattering, Stokes Raman Scattering, or Anti-Stokes Raman Scattering.

3.3 Nanoindentation

For nanoindentation test, there is not much restriction on dimensions, and hence the materials were sliced into smaller shapes compare with those used for phase identification. All the specimens used for nanoindentation test are in size around 5mm by 3mm in surface and 2 mm in height. However, there is an extreme requirement for surface roughness as well as the flatness of a specimen. Therefore, each specimen was polished double-sided with diamond lapping paper down to 15 um grades to ensure the flatness, and the flatness was determined by the bubble position in leveler relative to its center.

Aside from the specimen flatness, the surface roughness is especially crucial for nanoindentation test. Scratches at the surface may affect the contact between indenter tip and the specimen surface, and hence results in error within the early stage upon loading. To minimize the influence of surface roughness, all the specimens were polished in the same way that had been done before performing phase identification techniques. The only exception is for the last stage of polishing, the specimen had to be polished with 0.25 um water-based diamond suspension at 60 rpm for at least 20 hours to reach sufficient surface finish for nanoindentation test. Once polishing was done, the transparent epoxy was removed by placing the whole sample in an oven at 120℃ for 5 minutes. Later, the specimen could be set apart using spatula. The reason to remove the constraint by heat rather than solvent like acetone is to prevent the dissolved epoxy from forming a thin layer at the specimen surface and thus results in an error in nanoindentation test.

The nanoindentation test was performed with the assistance from Dr. George Pharr's student. Each sample was attached to a rigid aluminum pod with "crystal bond" to prevent any influence from substrate. To be specific, if the pod is not rigid enough, the measured stiffness

would be slightly off from the real value and then result in the error in the reduced modulus which can be calculated through the essential equation in nanoindentation. The load used in this work are 100 mN, 300mN, 500mN, 750mN, and 1000mN. The initial intent of this work was to study the cracking threshold; however, it is difficult to observe the indents of loads below 100mN due to the high hardness and elastic modulus of boron carbide. Should the cracking threshold of boron carbide be the main focus of this work, it is recommended to use cube corner indenter tip instead of Berkovich indenter tip. The loading and unloading rate of the indenter was kept at 25 mN/s for each material throughout the testing, and the Poisson ratio of 0.21 was set for the reduced modulus derivation. Constant Stiffness Measurement (CSM) was also employed in each testing, and thus the hardness values in terms of the displacement can be plotted. Before testing, the area function was calibrated using Oliver-Pharr's method on fused quartz [1]. All the mechanical properties extracted from nanoindentation testing were then plotted as a function of displacement and then discussed in **Section 4**.

3.4 Scanning Electron Microscopy (SEM) and Focused Ion Beam (FIB)

Scanning electron microscopy (SEM) was employed to study surface and subsurface cracks of indents. All the works, including focused ion beam (FIB), were done at Aggie Fab with Helios NanoLab 460F1, which is equipped with Ga-ion source. The images presented here were taken under Mode II immersion to resolve the edge contrast of cracks. The brightness and contrast of each image were fine-tuned to reveal the cracks, and thus some of the region in that image would appear over-exposed. Throughout the imaging, the electron beam voltage and current were kept at 10 kV and 10 nA, respectively. From the top view image of each indent, radial crack lengths were estimated and the indentation fracture toughness for each material was thus calculated based on the available models mentioned in **Section 2.3**.

Focused ion beam (FIB) was applied to precisely remove the material and then reveal the subsurface cracks beneath an indent [2-6]. In this work, the indents of 500 mN load are of interest for studying the surface and subsurface cracks at the same time due to the appropriate size of impressions for visualization. Because of the strong covalent bond between boron and carbon atoms in the material, the energy of the ion beam was set at its maximum value of 30kV and several beam currents were used, depending on the need for the work. In general, 9.2nA was applied for excavating a large trench under standard mode while 3nA for subsequent removal of material under cleaning cross-section mode. Specific attention was paid to several locations of an indent, namely radial crack tip, 50% of radial crack tip, corner of an indent, 50% toward the center, and lastly the center of an indent. **Figure 3.4** schematically displays these locations in an indentation impression. When approaching the above listed locations, lower current like 0.88nA was selected to avoid artifact and damage introduced by FIB process while not compensating the removal rate.

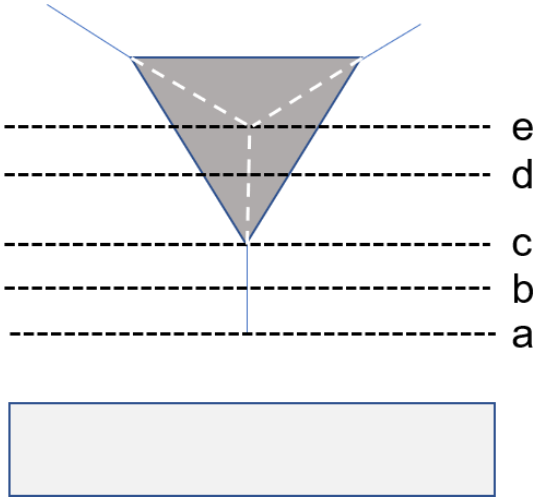

Figure 3.4 The schematic top view of the locations of interest in an indentation impression. The dash lines denote the slices at each specific location, with the alphabet on the right signifying the cutting orders. Note that the serial cross-sectioning always starts with excavating a large trench (shown as the grey box in the figure) in front of a radial crack tip at high beam current, and then successively mills into the impression at low current to avoid FIB-induced damage.

3.5 References

1. Warren C Oliver, G.M.P., *An improved technique for determining hardness and elastic modulus using load and displacement sensing indentation experiments.* Journal of materials research, 1992. **7**(6): p. 1564-1583.

2. Munroe, P.R., *The application of focused ion beam microscopy in the material sciences.* Materials Characterization, 2009. **60**(1): p. 2-13.

3. N. Cuadrado, J.S., D. Casellas, M. Anglada, E. Jiménez-Piqué *Geometry of nanoindentation cube-corner cracks observed by FIB tomography: Implication for fracture resistance estimation.* Journal of the European Ceramic Society, 2015. **35**: p. 2949–2955.

4. F. Lofaj, D.N., *Multiple cohesive cracking during nanoindentation in a hard W-C coating/steel substrate system by FEM.* Journal of the European Ceramic Society, 2017. **37**: p. 4379–4388.

5. Mound, B., *Cracking in Fused Quartz During Nanoindentation*, in *Materials Science and Engineering*. 2017, University of Tennessee. p. 165.

6. B. A. Mound, G.M.P., *Nanoindentation of Fused Quartz at Loads Near the Cracking Threshold.* Experimental Mechanics, 2019. **59**(3): p. 369-380.

4. RESULTS AND DISCUSSIONS

4.1 Phase Identification

The results regarding the chemical analysis of the materials were acquired with the following techniques, namely X-ray Diffraction (XRD) and Raman Spectroscopy.

4.1.1 X-ray Diffraction (XRD)

Figure 4.1 (a) shows the XRD results from each material. The XRD pattern of pure boron carbide is denoted as black line while the doped boron carbides are presented in red and blue. The star signs (*) in the figure point the peaks attributed to the boron carbide matrix and the open circle (○) marks the signal from graphite, which is commonly detected in sintered carbides. According to the Bragg's diffraction, a peak shift suggests either the compression or expansion in the corresponding diffracted lattice plane. Here indicates that the dopants were indeed doped into the boron carbide matrix. Meanwhile, from the result of Rietveld refinement, there are some unidentified peaks appeared in the pattern of doped samples, implying the presence of second phases. The magnified XRD patterns provide a better view at the peaks with the strongest intensity in each pattern. Interestingly, in B/Si co-doped boron carbide, the peak shift does not happen to every peak, suggesting that Si atoms only dwell at certain locations, and thus the structural expansion is not uniform throughout the matrix. On the other hand, with B doping alone, boron carbide demonstrates rather uniform expansion in crystal structure. The incorporation of dopants into the boron carbide matrix is again confirmed with Raman spectroscopy and the results are presented in the next subsection.

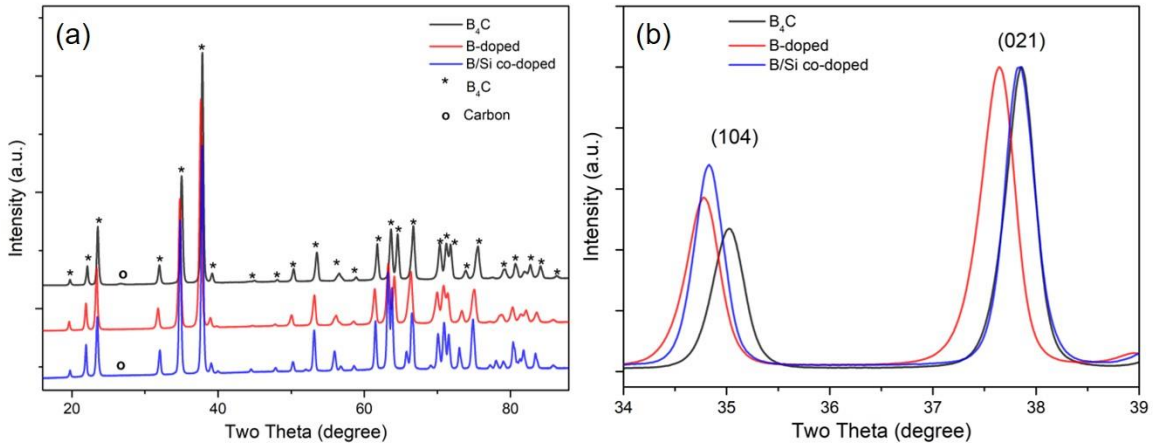

Figure 4.1 (a) The XRD patterns of pure boron carbide, B-doped boron carbide, and B/Si co-doped boron carbide. **(b)** The magnified view of peaks with strongest intensity to show the peak shift.

4.1.2 Raman Spectroscopy

The incorporation of dopants in the boron carbide matrix will affect the local chemical bonding, thus alter the lattice vibrational mode. The change can be captured via Raman spectroscopy in terms of the energy difference between incident and scattered photons, and the results are presented in **Figure 4.2**. Note that as previously stated, the attribution of certain Raman bands to corresponding vibrational modes is still under debate. Therefore, the results from Raman spectroscopy will only be presented for verifying the incorporation of dopants into the matrix.

As one can observe from **Figure 4.2**, the addition of boron and boron/silicon do alter the vibrational mode of the matrix, especially in the B/Si co-doped boron carbide. The most obvious difference appeared at around 300 cm^{-1} in B/Si co-doped sample, where the doublet was replaced with a single Raman band. This suggests that the presence of Si atoms in the matrix will affect the vibrational response of lattice in boron carbide. Perhaps Si atoms may help stabilize the disorder phonon responses upon interacting with the red laser.

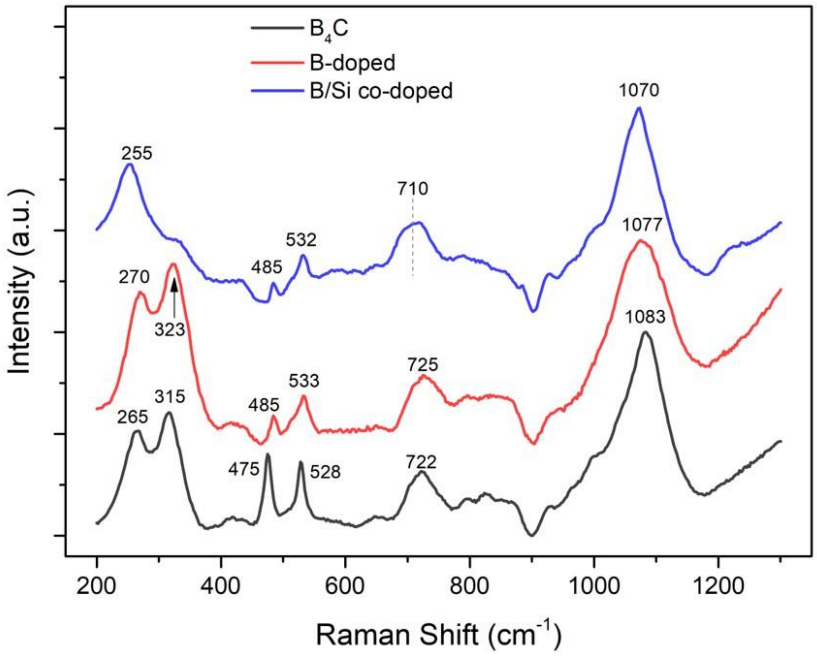

Figure 4.2 The Raman patterns of the three materials studied in this work. Note the disappearance of the doublet at 300 cm^{-1} in B/Si co-doped boron carbide. The presence of Si in the matrix may help suppress the disorder phonon response in boron carbide.

Apart from the apparent change in B/Si co-doped boron carbide, the shift in Raman bands also indicates the foreign atoms incorporating in the superlattice of boron carbide. In general, the blue-shift (to the right) in a Raman band means higher vibrational energy state, which may rise either from shorter bond length or under compression. Here in this study, the Raman bands 475 cm^{-1} and 528 cm^{-1} shift to higher wavenumbers suggest that the corresponding lattice vibration become more vigorously. On the other hand, the red-shift (to the left) in the 1083 cm^{-1} Raman band is suppressed. To summarize, the change in the lattice vibration can serve as an indication of the incorporation of foreign atoms into the matrix, and such lattice response can be captured by Raman spectroscopy.

4.1.3 Summary

Starting from the XRD results, the shift in the diffracted peaks indicates the lattice expansion caused by dopants. Similarly, the shift in Raman bands also confirms the presence of foreign atoms in the boron carbide matrix, thus altering the vibrational energy state. The most striking change was observed in the Raman pattern of B/Si co-doped boron carbide where the doublet at 300 cm^{-1} was replaced with a single Raman band. With the structural analyses presented in this section, the latter mechanical testing should be representative to each material.

4.2 Nanoindentation

In this section, the author will focus on the analysis and interpretation of the load-displacement data and those obtained through Continuous Stiffness Measurement (CSM). For each material, the mechanical properties acquired from the nanoindentation testing were summarized in **Table 4.1**. The analysis regarding nanoindentation induced cracking will be addressed in **Section 4.3** and **Section 4.4**.

Table 4.1 Summary of Hardness and Elastic Modulus of Each Material

Materials	**B_4C**	**B/Si co-doped**	**B-doped**
Hardness (GPa)	46.53 ± 1.13	42.60 ± 2.91	44.72 ± 2.43
P Value	N/A	7.26×10^{-15}	8.55×10^{-7}
Elastic Modulus (GPa)	515.52 ± 10.38	493.04 ± 34.60	496.09 ± 12.17
P Value	N/A	5.97×10^{-6}	1.28×10^{-15}

4.2.1 Hardness Measurements

Because of CSM, the hardness of a material can be monitored throughout the loading of nanoindentation test and thus can be plotted as a function of displacement. In **Figure 4.3,** the second row shows the examples of the hardness versus displacement relationship of each material. The hardness values of each material summarized in **Table 4.1** were exported from the range of 200 nm to 300 nm in displacement due to the indentation size effect as well as the initial burst of the hardness value happened in pure boron carbide and B/Si co-doped boron carbide. Apart from that, the huge drop in hardness value after the burst is associated with the first pop-in event, as shown in **Figure 4.3**. The measured hardness values are close to those have been reported [1-4]. It can be observed that the additional B and/or Si atoms in the matrix results in lower hardness values. Xie *et al.* has suggested that in boron carbide the B-C bond is stronger than B-B bond [3]. By adding more B into the matrix, the amount of B-C bond is decreased, thus yielding lower hardness values of the material. Similarly, Khan *et al*. suggested that the Si dopant would replace the chain center position, which also reduced the amount of B-C bond in the material [5]. Following the same concept, the decrease in the hardness value of B/Si co-doped boron carbide is expected.

In addition to the values, the shape of the curves from pure boron carbide and B/Si co-doped boron carbide is different from that of B-doped boron carbide, as shown in **Figure 4.3**. The author believed that the apparent difference in the shape stemmed from the different processing methods. In this work, pure boron carbide and B/Si co-doped boron carbide were both fabricated through hot-pressed sintering while the B-doped sample was made via spark plasma sintering (SPS). The major difference in these two methods is the processing time, with the former one longer than the latter. Grain growth is one of the material phenomena that may arise

from the prolonged processing time. Therefore, the author speculated that the difference in the grain size is the main cause of the different shapes of the curves. Despite of that, more experiments should be done to prove the speculation.

4.2.2 Elastic Modulus Measurements

With the aid of CSM, the elastic modulus can be monitored throughout the loading, and results of each material was summarized in **Table 4.1**. The plot that shows the relationship with indentation displacement is presented in **Figure 4.3**. Unlike the hardness to displacement plots, the elastic modulus to displacement plots appear similar to each other, and again a drop in the value can be observed at where a pop-in event is detected. The mechanism behind the technique is that pop-in event corresponds to sudden loss in stiffness measurement. As an indenter being driven further into the sample, the measured stiffness returns to normal until the next pop-in happens.

Despite that the elastic modulus is rather independent of indentation displacement, to maintain the consistency with **Section 4.2.1**, the data exporting range was set as 200 nm to 300 nm in displacement. The measured elastic modulus of pure boron carbide is close to those have been reported in literature [1]. As for the doped boron carbide, there is no much data available, however a trend of decreasing elastic modulus for doped boron carbide is expected since the number of strong covalent B-C bond decreases as dopants being added into the matrix [3]. The similar concept was also observed in the hardness measurement.

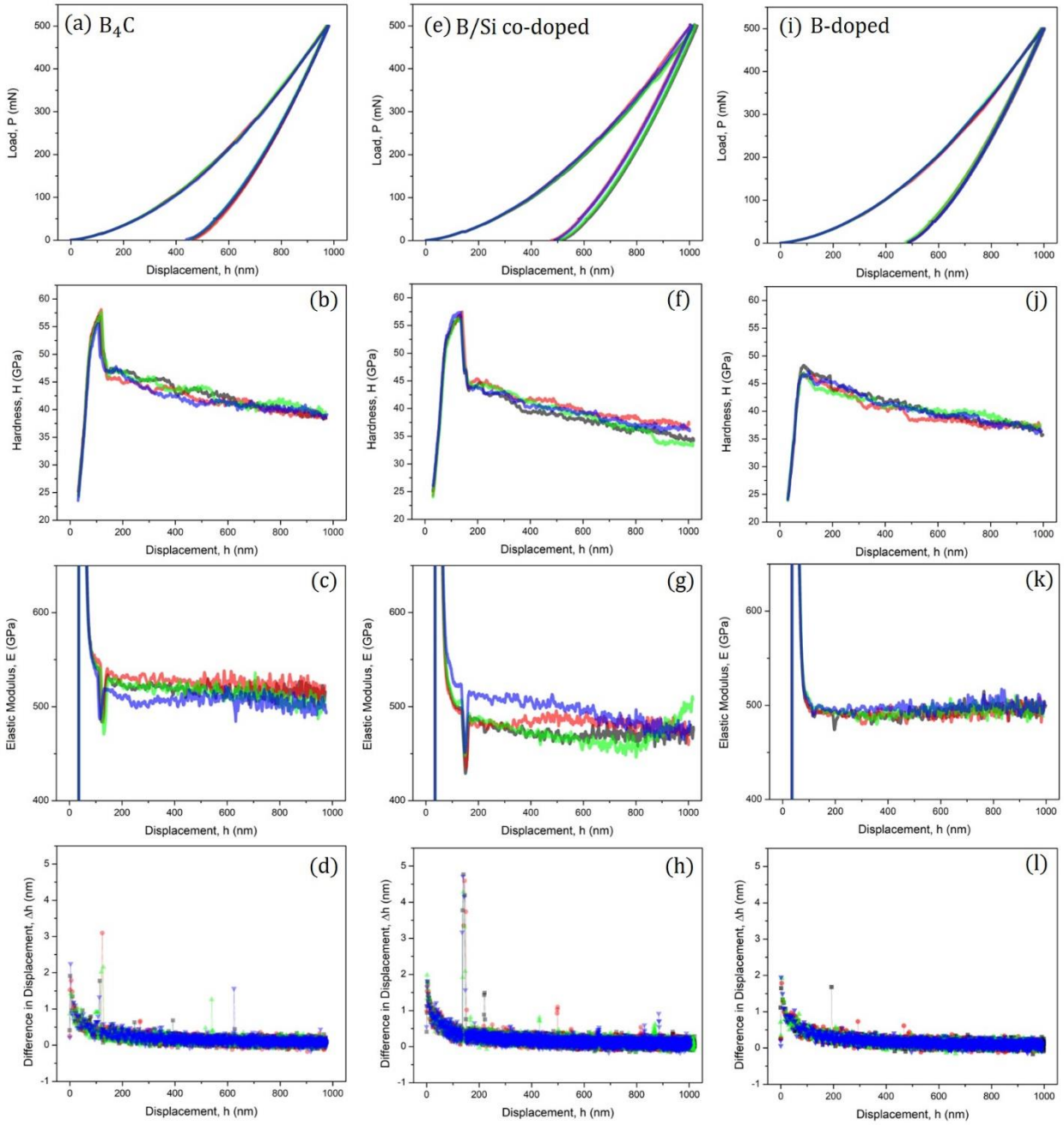

Figure 4.3 (a), (e), and **(i)** presents the representative load-displacement curves at 500mN load for each material. The following figures in the same column are the corresponding hardness, elastic modulus, and pop-in detection plots as a function of displacement for each material.

4.2.3 First Pop-in Events

In the analysis of the load-displacement data, the specific attention was paid to the detection for the first pop-in events in the boron carbide samples. As discussed in **Section 2**, the physical origin of pop-in events in brittle materials is of important when it comes to fine-tuning the micro-machining parameters in various engineering applications. **Figure 4.4** presents the enlarged view of the first pop-in events in **Figure 4.3 (a)**, **(e)**, and **(i)**. Here we can observe that the first pop-in event in pure boron carbide and B/Si co-doped boron carbide occurs in the earlier stage of loading (~20mN) whereas that of B-doped boron carbide happens around 30mN. To assure that the results presented here is representative, the author re-visited all the 500mN tests of each material and provided the distribution of the corresponding load of the first pop-in event in each material, as shown in **Figure 4.5 (a)**. The occurring ranges for pure boron carbide and B/Si co-doped boron carbide are close to each other, with the averaged occurring load of the latter one slightly higher than the former one by 3.01mN. On the contrary, the occurring range of the first pop-in event for B-doped boron carbide is relatively stochastic, and more than half of the tests do not show the apparent discontinuities during loading. To understand the physical origin of the first pop-in event, lower loads such as 10mN and 30mN were applied for pure boron carbide. As shown in **Figure 4.6 (a)**, the load-displacement curve for 10mN testing exhibits fully elastic behavior, whereas the slight deviation between the loading and unloading curves originates from the environment, for example, thermal drift and vibration from the machine. As soon as the load applied to the material exceeds 10mN, pop-in event occurs. Therefore, pop-in event can be viewed as the onset of plasticity in pure boron carbide.

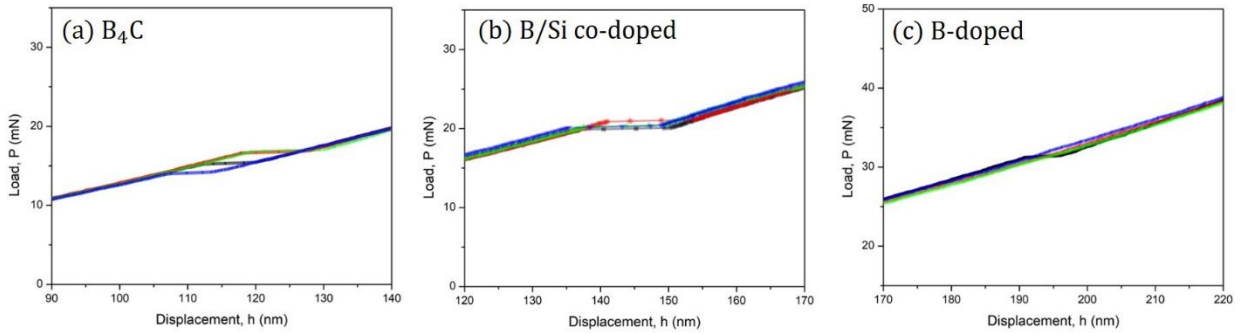

Figure 4.4 The enlarged view of the first pop-in events in **Figure 4.3 (a)**, **(e)**, and **(i)**. Note that for B-doped boron carbide, the first pop-in event takes place in a stochastic manner, and here shows the only one that occurs in low load.

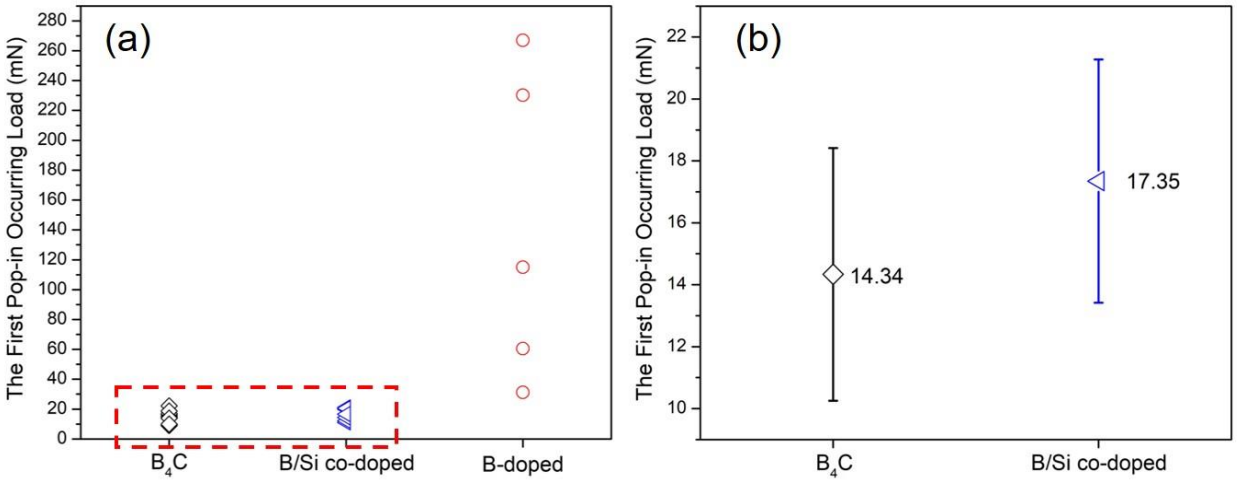

Figure 4.5 (a) The distribution of the corresponding load at the first pop-in event in each 500mN test. **(b)** The averaged occurring load of the first pop-in event in pure boron carbide and B/Si co-doped boron carbide.

As discussed in **Section 2**, dislocation nucleation rarely occurs in brittle materials when accommodating the imposed strain, instead phase transformation [6], twinning [7], and cracking [8] are more commonly observed. In boron carbide, phase transformation and cracking are the two main mechanisms for dissipating energy. To calculate the shear stress required for the plasticity to initiate, the method proposed by Page *et al.* was applied [9]:

$$\tau_{max} = 0.12 \times \sqrt[\frac{1}{3}]{\frac{P_{crit}{E_s}^2}{{R_{eff}}^2}} \quad \text{(Eq 4.1)}$$

where P_{crit} is the load where the pop-in event initiates, E_s is the elastic modulus of the indented sample, and R_{eff} is the effective radius derived from the elastic portion of a load -displacement curve via Hertzian contact fitting, as demonstrated in **Figure 4.6 (b)**. From Eq. 4.1, the resultant maximum shear stress in the low load testing for pure boron carbide is 25.94 ± 0.57 GPa, which is close to the reported values required for amorphization to take place [1, 10].

Although the low load testing was only performed on pure boron carbide, similar analysis can also be applied to B/Si co-doped carbide. Despite that the results may not be as accurate as that for pure boron carbide, it still provides a trend on how the dopants affect the shear stress induced by nanoindentation. The shear stress induced in B/Si co-doped boron carbide is 24.47 ± 0.52 GPa, which is slightly lower than that of pure boron carbide. This is expected due to the reduced amount of strong covalent bond (B-C bond) in the doped boron carbide. Unfortunately, such method could not be applied to B-doped boron carbide as there was no apparent discontinuity in the low load ranges, meaning that plasticity might have occurred in the material prior to the pop-in event. Therefore, the elastic analysis based on Hertzian contact is not valid in this scenario. More analyses on the effect of dopants will be discussed latter.

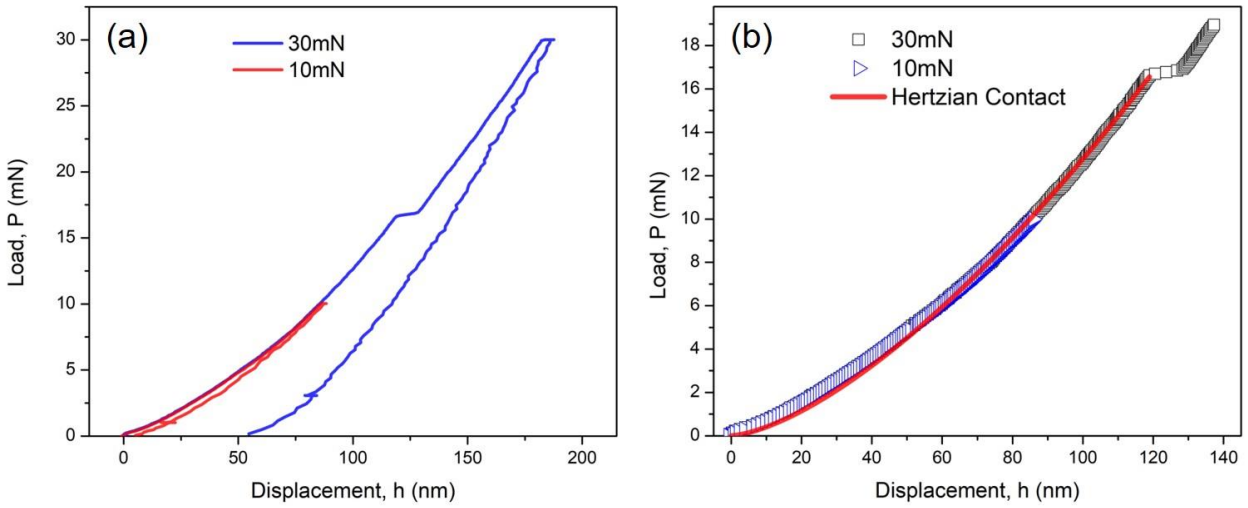

Figure 4.6 (a) The representative load-displacement curves of 10mN and 30mN nanoindentation testing on pure boron carbide. **(b)** The Hertzian contact fitting of 30mN curve prior to the pop-in event.

4.2.4 The Effect of Dopants on the Mechanical Properties

The aforementioned results indicate that the incorporation of foreign atoms in the boron carbide matrix will lead to a lower hardness value and elastic modulus. This is primarily due to the decreasing number of strong covalent B-C bond in the material. By looking at the nominal chemical composition of the doped boron carbide, the major loss in the B-C bond results from the additional boron atoms in the matrix, whereas the content of Si is only 1.5 at%. Still, with the minute amount of Si addition, the hardness and elastic modulus of the material further decrease by 2.12 GPa and 2.05 GPa, respectively. However, as widely reported and accepted in the boron carbide community, despite of losing some of the mechanical properties, the formation of the amorphized phase can be inhibited by doping. With the Raman mapping technique, Khan *et al.* [5] and Yang *et al.* [11] had proved that Si atom can mitigate the amorphization in boron carbide when subjected to Vickers indentation. The mechanism behind the mitigation was believed that Si atom would form an extra bond with the neighboring icosahedral boron atom, thus improving

the stability of the chain structure, which was previously considered vulnerable to shearing and later became the origin of amorphization [5]. In this work, the mitigation of amorphization manifests in the delay of pop-in event, with the averaged occurring load of B/Si co-doped boron carbide is higher than that of pure boron carbide by 3.01mN. This additional tolerance to pop-in event suggests that the plasticity in B/Si co-doped boron carbide requires more energy to initiate, and therefore it is expected that this material will exhibit higher indentation fracture toughness than its pure counterpart does.

4.2.5 Summary

From the data acquired via CSM, all materials exhibit indentation size effect, meaning that the measured hardness value is dependent on the indentation displacement. This phenomenon arises from that larger the contact volume, the higher chance of encountering defects, for example porosity, thus resulting in a lower hardness value. Note that elastic modulus is rather independent of the displacement. Another thing that can be observed from the data is that the sudden drop in the measured values corresponds to the pop-in event in each nanoindentation test. The physical origin of the pop-in event in boron carbide was believed to be amortization and cracking as according to literature, dislocation nucleation is unlikely to happen in boron carbide system due to strong covalent bonding. The results suggest that B/Si co-doped boron carbide requires more energy for plasticity to initiate than pure boron carbide does, which can be inferred from the averaged pop-in occurring load of these two materials. As for B-doped boron carbide, there is no apparent discontinuity in most of the nanoindentation test, and therefore the same analytical approach cannot be applied to it.

4.3 Surface Cracking

In this part of the thesis, the SEM images of nanoindentation-induced surface cracks in three different materials are presented, and the length of cracks and the size of the impression were measured via the image-processing software, ImageJ. Note that only 500mN-load indents are included in this subsection due to the pandemic that prevents graduate students from doing experiments. **Figure 4.7** defines the crack length and the size of an indentation impression. The measured values were summarized in **Table 4.2** and were later applied for calculating the indentation fracture toughness of the three materials.

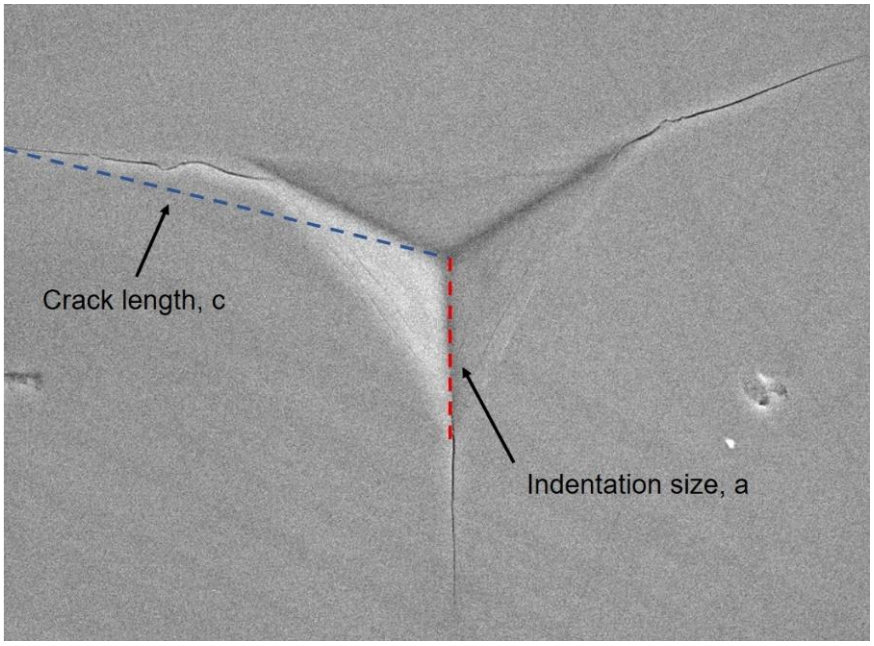

Figure 4.7 Crack length (c) and indentation size (a) measured from indentation. For each impression, all three crack lengths and indentation sizes were measured and averaged. Note that the crack length, c, is measured from the center of the impression to the radial crack tip, regardless whether it comes off from the corner of the impression.

Table 4.2 Summary of the crack lengths and indentation sizes

Materials	B_4C	B/Si co-doped	B-doped
Indentation Size, *a* (μm)	3.43 ± 0.09	3.41 ± 0.24	3.39 ± 0.08
P Value	N/A	0.45	0.49
Crack Length, *c* (μm)	5.95 ± 0.89	6.47 ± 0.66	4.36 ± 0.39
P Value	N/A	0.083	5.91×10^{-5}

4.3.1 Pure Boron Carbide (B_4C)

Figure 4.8 demonstrates the representative indentation impressions at 500mN load on the pure boron carbide sample, which will serve as the base-line for analyzing the doped boron carbide samples. As shown in the figure, all the impressions possess three radial cracks emanating either from the corners or from the side, which are a typical feature of crystalline brittle materials subjected to nanoindentation. One feature worth notice is that the fringes of an impression slightly curve inward, indicating an indentation phenomenon called sinking-in. This feature is commonly observed in brittle materials or, specifically by material properties, low E/H value materials [12]. Another feature along the fringes of an indentation impression is edge crack. Yoshida *et al.* had proposed the physical explanation to the edge cracking based on their in-situ observation of nanoindentation in soda-lime glass. For Berkovich indenter tip, the edge crack occurs during loading in which the local tensile stress generated by the sinking-in triggers the cracking along the fringe of an impression [8].

From the representative impressions, the radial cracks appear either straight or tortuous. In amorphous brittle materials, which show isotropic mechanical properties, it is common to observe a straight radial crack coming off the corner of an impression. However, for crystalline

materials, the anisotropy in the mechanical properties will lead to preferred cleavage planes, and thus one can observe a sudden change in the direction of the crack. Interestingly, in pure boron carbide, both types of radial crack were formed. To the best of the author's knowledge, boron carbide does not show preferred cleavage plane during cracking, at least not being reported so far. With that being said, the anisotropy in mechanical properties of boron carbide plays a minor role than that does in other brittle materials, for example sapphire [7, 13]. However, to verify such statement, it is recommended to study the crystallographic orientation of each impression.

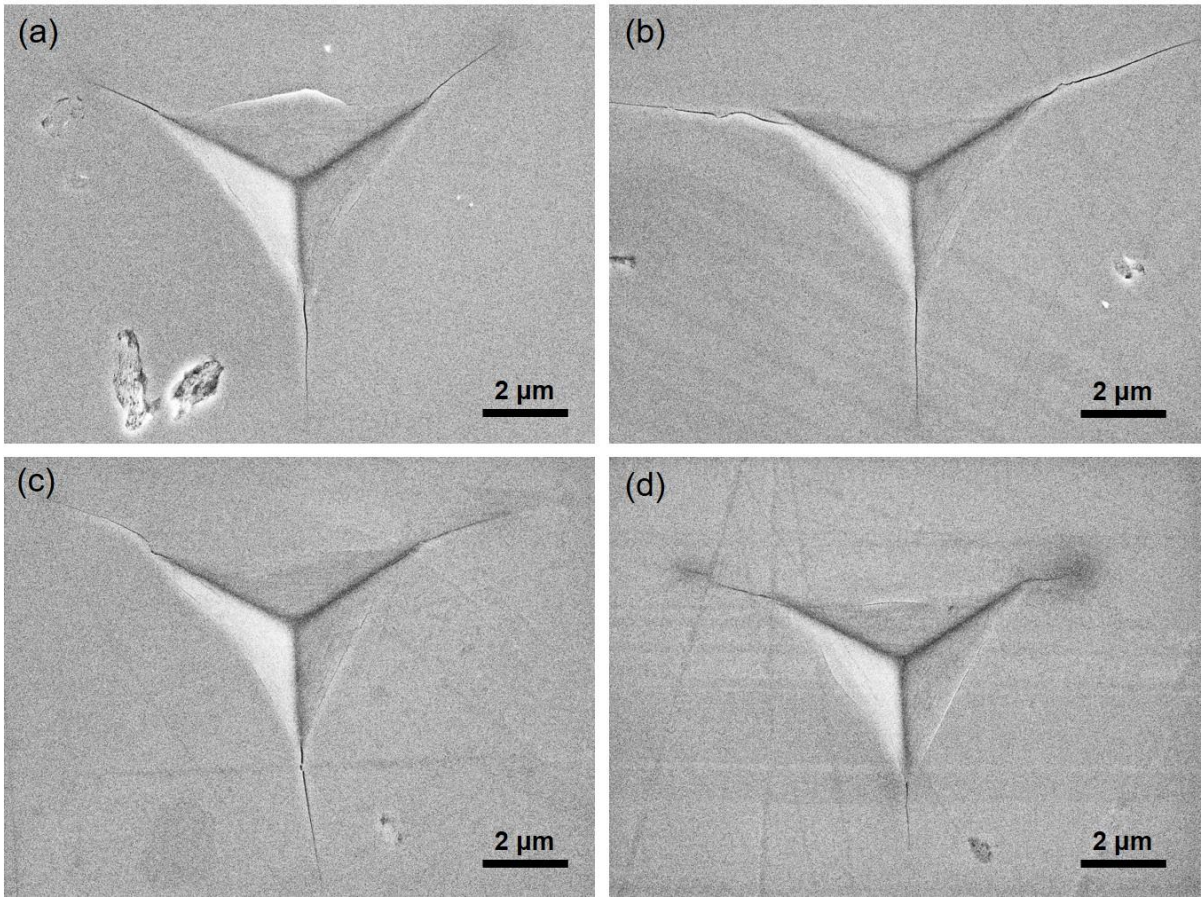

Figure 4.8 The representative indentation impressions at 500mN load on pure boron carbide. Note that in some impressions, chipping can be observed at the edge. Cook et al. suggested that this may resulted from the subsurface lateral cracks propagating to the surface [12].

4.3.2 Boron-doped Boron Carbide

The representative indentation impressions of B-doped boron carbide sample are presented in **Figure 4.9**. Compared with that of pure boron carbide, there is no much difference in the indentation size but the radial cracks are generally shorter. Even in some of the cases, as shown in **Figure 4.9 (b)**, the absence of a radial crack was observed. These impressions were discarded in the crack length measurement and were not included in the later indentation fracture toughness calculation. Despite appeared short, the radial cracks in B-doped boron carbide are usually tortuous, and there are more radial cracks emanating from the fringe. This suggests that elastic anisotropy may play a role in crack propagation. However, it is necessary to investigate the crystallographic orientation of each impression to justify the statement.

In addition to radial cracks, edge cracks also appeared in B-doped boron carbide. This type of crack might be initiated by the tensile stress caused by the sinking-in during loading, as proposed by Yoshida and co-authors [8, 14]. Another feature worth notice in the B-doped boron carbide sample is that there are more porosities than that in the pure boron carbide sample. It is probably due to the nature of short processing time in spark plasma sintering (SPS) that does allow the material to fully densify. Therefore, it is expected that porosity will be more prevalent than in the other two materials that were fabricated through hot-press sintering. In fact, the presence of porosity in the B-doped boron carbide sample largely affect the estimation of indentation fracture toughness. This will be discussed in detail in **Section 4.3.4**, and the results presented in **Section 4.4.5** will further justify the statement.

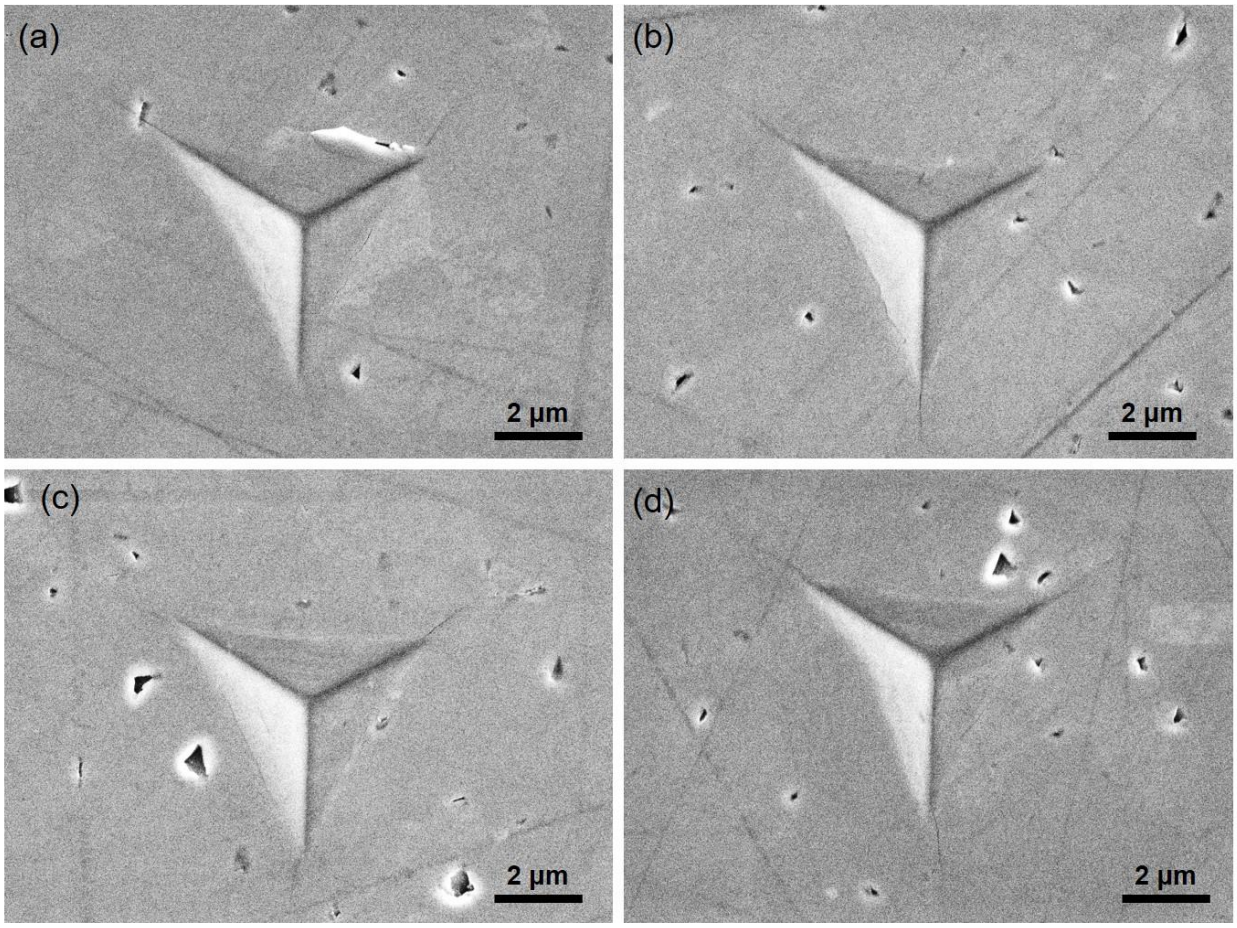

Figure 4.9 The representative 500mN-load indentation impressions of B-doped boron carbide. Note that the radial cracks are generally shorter than that in pure boron carbide. Also, there are more porosities in the material, suggesting that crack propagation may be hindered due to the crack tip blunting.

4.3.3 Boron/Silicon Co-doped Boron Carbide

The representative 500mN-load indentation impressions of B/Si co-doped boron carbide are presented in **Figure 4.10**. Note that the black faceted features near an impression indicate the presence of secondary phase other than graphite. In most of the cases, these inclusions have minor effect on the nanoindentation data, while in some of the tests, it is found that the indenter stroke directly into the secondary phase and caused unexpected cracking. These impressions were considered invalid and were discarded from the latter analyses.

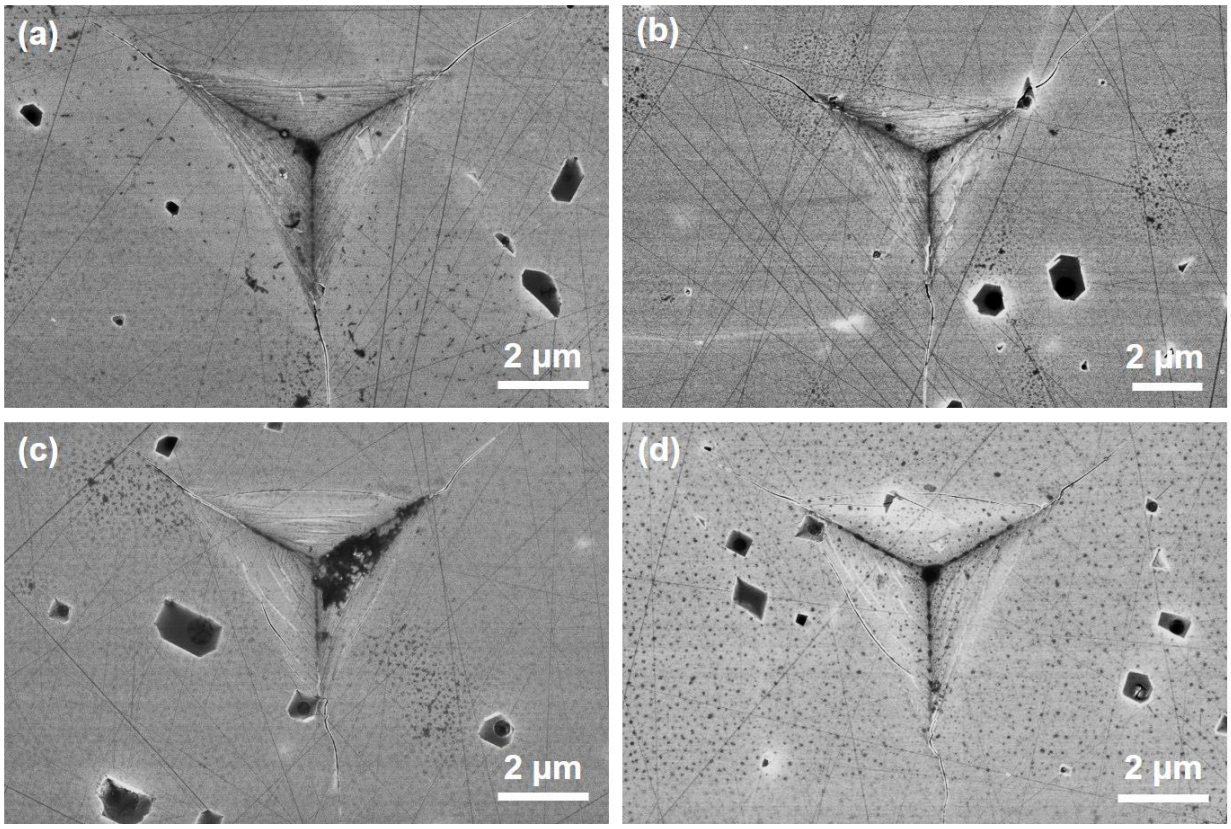

Figure 4.10 The representative 500mN-load indentation impressions of B/Si co-doped boron carbide. The black faceted features in the figure indicate the presence of secondary phase other than graphite. From the results, the secondary phase does not influence the indentation response of B/Si-co-doped boron carbide.

Compared with that in the other two materials, there is no apparent difference in the size of the impression in B/Si co-doped boron carbide, and meanwhile the morphology of the surface cracks is close to that of pure boron carbide. Similarly, the radial cracks in B/Si co-doped boron carbide appear either straight or tortuous, implying the influence of crystallographic orientation in the cracking behavior. Apart from that, edge cracks also happened in B/Si co-doped boron carbide, and they are more prevalent than that in pure boron carbide. By careful observation at the distribution of the slip bands inside an impression, it is proposed that these features are related to the edge cracks. A direct approach to study their relationship is via focused-ion beam

cross-sectioning to see whether the slip bands develop into edge crack. A detailed observation will be presented in the next section.

4.3.4 Estimated Indentation Fracture Toughness

As suggested in **Section 2.3**, the calculation of indentation fracture toughness will be based on the model proposed by Lawn and co-authors [15], with the modified pre-factor, α, following the analysis by Jang and co-authors [16]:

$$K_c = \alpha \left(\frac{E}{H}\right)^{\frac{1}{2}} \frac{P}{c^{3/2}} \quad \text{(Eq. 4.2)}$$

$$\alpha = \frac{0.0352}{1-\nu} \left(\cot\psi\right)^{\frac{2}{3}} \quad \text{(Eq. 4.3)}$$

where E, H, P, and c are the elastic modulus, hardness, applied load, and crack length, respectively. For the expression of the pre-factor, ν and ψ are the Poisson's ratio and the center line-to-face angle of the indenter tip, respectively. In this work, the Poisson ratio of the three materials are set as 0.21, and the half-included angle for the Berkovich indenter tip is 65.27˚, thus yielding 0.0256 for α. The indentation fracture toughness for each material are summarized in **Table 4.3**.

Table 4.3 The indentation fracture toughness for the undoped and doped boron carbide.

Materials	**B_4C**	**B/Si co-doped**	**B-doped**
Indentation Fracture Toughness ($MPa \cdot m^{1/2}$)	3.15 ± 0.65	2.79 ± 0.39	4.91 ± 0.66
P Value	N/A	0.031	3.24×10^{-10}

The calculated indentation fracture toughness of pure boron carbide is higher than what have been reported using Vickers indentation [1-3]. This perhaps stems from that in micro-indentation, there is higher chances to encounter defects in the material which may act as stress concentration site, thus resulting in lower indentation fracture toughness. On the contrary, because of the small probing volume in nanoindentation, the indentation response mostly comes from a single grain, and thus the intrinsic material properties should play a major role in cracking resistance. Therefore, it is expected that the values we obtained in this work would be higher than those derived from micro-indentation testing.

From **Table 4.3**, it is indicated that the indentation fracture toughness of B-doped boron carbide is anomalously higher than the other two materials. In fact, the expression listed above suggest that the indentation fracture toughness would be higher with short crack lengths, however, from **Figure 4.9**, micro-pores are present at the surface, and that will cause the blunting of a crack tip, thus hindering the propagation. Therefore, the obtained values would be overestimated. Aside from that, the Lawn, Evans, and Marshall Model (LEM) assumes half-penny crack beneath the impression and does not account for the contribution from the edge crack and the lateral crack, even though Jang *et al*. had modified the model to accommodate the three-sided Berkovich tip. With that being said, the actual energy required to initiate cracking should be lower than the estimated values for the three materials.

4.3.5 The Effect of Dopants on the Estimated Indentation Fracture Toughness

From the results presented in **Section 4.2**, it is proposed that the addition of dopants in the boron carbide matrix could delay the occurring load of the first pop-in event by mitigating the formation of amorphous bands, and meanwhile more energy is required for plasticity to initiate in B/Si co-doped boron carbide, assuming that the first pop-in event is associated with the

transition from purely elastic to elastic/plastic deformation. Here the proposition to the first pop-in event will be discussed in terms of direct observation of the surface cracks. Note that the following discussion will exclude B-doped boron carbide as the cracking behavior is unexpected and needs another round of testing in the future to assure the repeatability.

From the crack length and the indentation impression size measurements presented above, the incorporation of foreign atoms in boron carbide matrix has little effect on the size of the indentation impressions, however, there is an apparent difference in the crack lengths. As shown in **Figure 4.8** and **Figure 4.10**, the crack lengths appear longer in B/Si co-doped boron carbide, compared with the baseline material, pure boron carbide. This is probably due to the decrease in the number of strong B-C covalent bond, as proposed by Xie and co-authors [3]. The lower indentation fracture toughness of B/Si co-doped boron carbide could support the proposition that the energy required for the cracking to initiate in this material is lower than that in its undoped counterpart. Meanwhile, in the analysis of the first pop-in event, B/Si co-doped boron carbide could absorb more energy prior to the discontinuity appeared in the load-displacement curve. This may explain why the cracking is more severe in B/Si co-doped boron carbide, given that more energy is absorbed and the resistance to cracking is inferior to pure boron carbide.

To sum up, despite the intrinsically weaker in the resistance to cracking, the addition of dopants in the boron carbide matrix could withstand more energy prior to the crack initiation than the pure boron carbide does via mitigating the formation of amorphous bands during impact.

4.3.6 Summary

A detailed analysis of the surface cracks induced by 500mN-load nanoindentation in each material was conducted, and the results are discussed and presented in this section. From the indentation impression size and crack length measurements, there is no apparent difference in the size of the indentation impression but a substantial difference in the crack lengths is observed. Note that the crack length of B-doped boron carbide is anomalously higher than the other two, thus being excluded in the latter analysis. It is probably due to the short processing time in SPS that does not allow the material to fully densify. Therefore, micro-pores were observed in the material, which could hinder crack propagation and render the indentation fracture toughness overestimated.

From the comparison between the other two materials, it is suggested that the addition of the dopants in born carbide matrix could increase the energy required for the onset of plasticity in spite of the weaker intrinsic resistance to cracking.

4.4 Subsurface Cracking

From the previous analysis of the indentation fracture toughness, it was found that the applied model does not account for the edge crack and lateral crack. Also, it remains unclear whether the crack morphology in the studied materials follows the assumed half-penny crack. Therefore, focused-ion beam (FIB) was employed to study the subsurface cracking in the three materials. To maintain consistency, the 500mN-load indentation impressions were selected for FIB cross-sectioning, and for each impression, there are five positions of interest, namely radial crack tip, 50% radial crack, corner of the impression, halfway from corner toward center, and finally, the center of the impression, as shown schematically in **Figure 3.4**.

4.4.1 Pure Boron Carbide (B_4C)

The subsurface cracks of 500mN-load indentation impression in pure boron carbide are presented in **Figure 4.11**. To begin with, as shown in **Figure 4.11 (a)**, the position initially denoted as the radial crack tip from the surface view is in fact not the actual crack tip since the subsurface crack is already present at a certain depth. This indicates that the very front portion of the radial crack has yet propagated to the surface, thus resulting in the over-cut of the radial crack tip. Note that there is a faint feature near the crack propagating straight down to the material. That is the artifact caused by FIB, which in some of the similar studies will mix up with the actual crack [17, 18]. Fortunately, the subsurface cracks in pure boron carbide are tortuous, and thus the FIB artifacts are discernible.

In **Figure 4.11 (b)**, at the nominal halfway of the radial crack, the subsurface crack appears tortuous and is off away from the centerline, despite it being straight from the surface view. This implies the influence of crystallographic orientation on the cracking behavior. Note that the subsurface crack had propagated deep into the material where could not be captured in the view field. The faint feature ensuing the apparent tip of the subsurface crack is actually the part of the crack as referred. A reason not able to resolve that portion is probably due to the nature of FIB, in which the ion beam can only be focused at the surface. Once beyond the focusing plane, the ion-beam starts to diverge, and thus the etching rate is no longer assured. Another reason may be that the crack was filled by the removed material during FIB slicing. So far, the observation of the radial crack is close to what Cuadrado *et al.* had found in various brittle materials that the subsurface cracks are not straight down into the material [19].

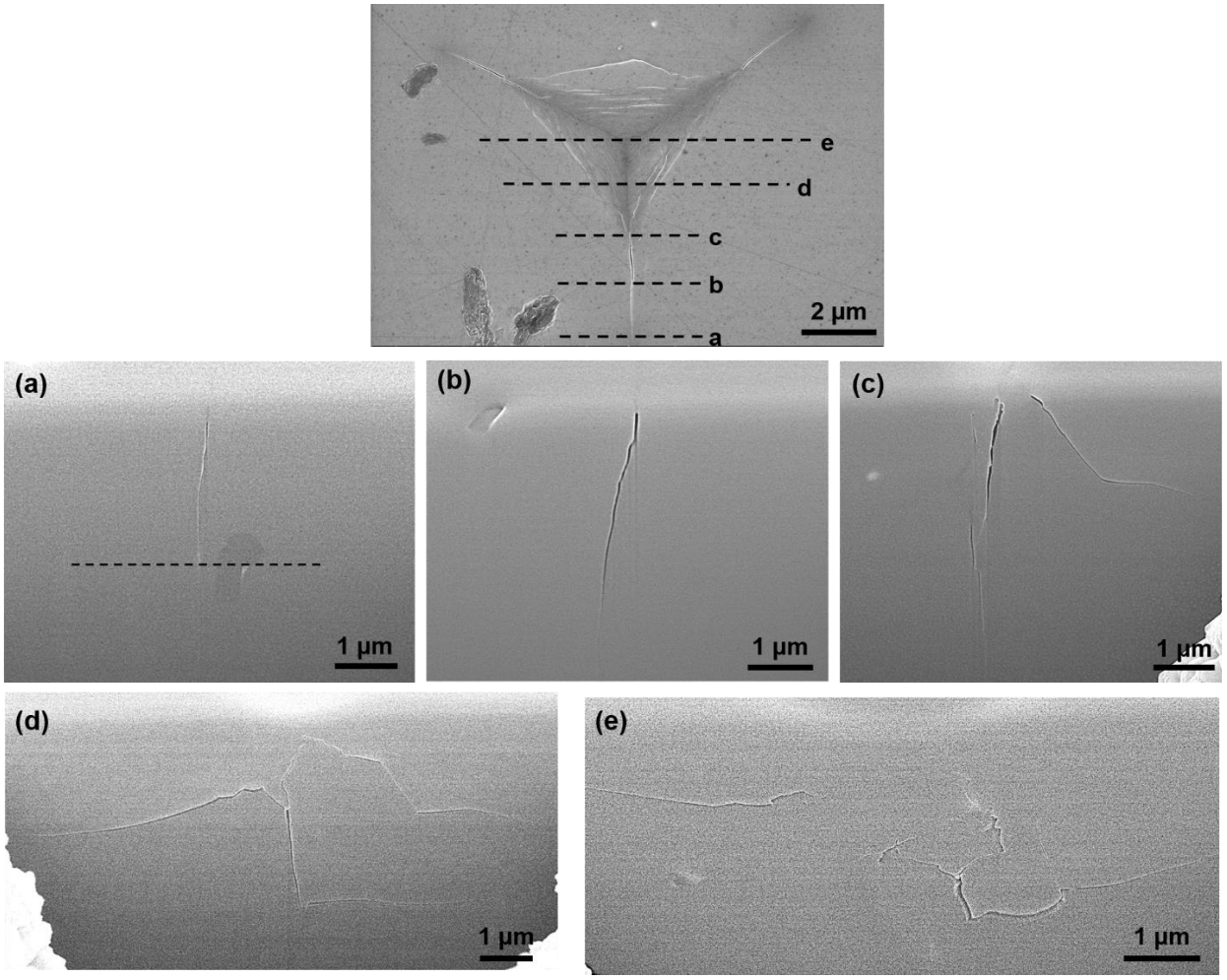

Figure 4.11 The cross-section of the selected positions of 500mN-load indentation impression in pure boron carbide. The dash line in **(a)** denotes where the subsurface crack terminates. Note that in **(c)**, a crack initiates from the edge crack, as indicated by the black arrow.

As the FIB process approached to the corner of the impression, as shown in **Figure 4.11 (c)**, a subsurface crack propagating from the surface and then turning into lateral direction was captured. By close observation, it can be inferred that this crack initiated from the edge crack at the surface, as the black arrow pointing at in the figure. As for the primary subsurface crack, the cracking became more severely and again extended beyond the view field.

In **Figure 4.11 (d)**, the FIB process arrived at the halfway from the corner toward the center of the impression. At this location, it can be observed that the lateral crack developed from the median crack, assuming the half-penny crack formed beneath the impression. Also, the as-mentioned secondary subsurface crack coalesces with the primary one, suggesting that the previous proposition that this crack initiated from the edge crack is incorrect. Another feature as shown in this figure is that the primary crack did not further extend down into the material, instead it stopped at certain depth and then started to propagate in the lateral direction. This type of propagation has not yet been reported for brittle materials, and therefore another round of FIB cross-sectioning is needed to justify whether it is representative.

The cross-section view of the subsurface crack at the center of the indentation impression is presented in **Figure 4.11 (e)**. Surprisingly, there is no median crack present at this location; instead, the cracks propagate in the lateral direction. Right beneath the impression, there is a region free of cracks, suggesting the zone with residual compression. The boundary along which the subsurface crack initiates from is denoted as the elastic/plastic boundary, and it can also be inferred that there is a transition from compression to tension in the local stress field, thus the cracking being promoted.

4.4.2 Boron-doped Boron Carbide

Figure 4.12 presents the SEM images of the subsurface cracks at the selected locations of a 500mN-load indentation impression in B-doped boron carbide. Note that most of the impressions in this material exhibit relatively short radial crack lengths, thus the one presented here was chosen simply because of its appropriate dimension for handling.

Similar to the finding in **Figure 4.11 (a)**, the subsurface crack shown in **Figure 4.12 (a)** has no surface trace. Still, the subsurface crack appeared short and faint, indicating the fact that the location is indeed close to the actual radial crack tip. Apart from that, the subsurface crack does not propagate straight down into the material, suggesting that the influence of crystallographic orientation on the cracking behavior. **Figure 4.12 (b)** shows the morphology of the subsurface crack at the mid-point of the radial crack. It can be observed that there is no apparent difference with that in the last location except for the dimension.

In **Figure 4.12 (c)**, micro-pores were captured by the SEM imaging. This finding supports the previous postulation on the anomalously higher indentation fracture toughness in B-doped boron carbide, although the figure does not show the crack arrested by the micro-pores. As the process moving forward to the center, the subsurface crack exhibit like a perfect median crack which propagates straight down into the material, as shown in **Figure 4.12 (d)**. However, as signified with the black arrow, there is a lateral crack emanating from the median crack. This additional subsurface crack is not considered in Lawn, Evans, and Marshall's indentation fracture toughness model [15], thus resulting in the overestimated values in this content.

Eventually, the FIB process arrived at the center of the impression, as shown in **Figure 4.12 (e)**. Out of expectation after observing a near-perfect median crack, there is micro-pore right

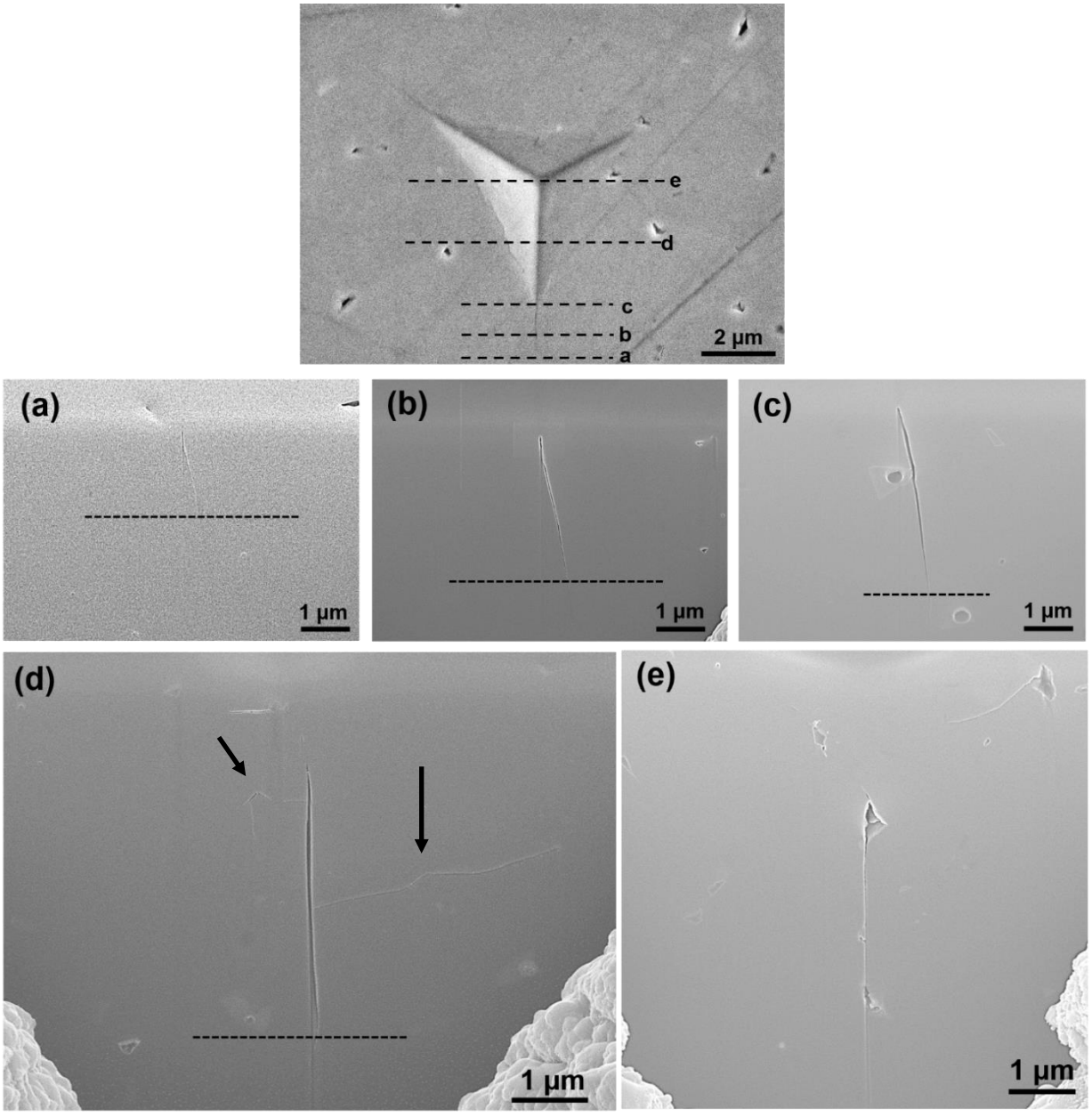

Figure 4.12 The cross-sectional view of the subsurface cracks at selected locations of a 500mN-load indentation impression. The black dash line in **(a)**, **(b)**, **(c)**, and **(d)** denotes where the crack terminates. Note in **(e)**, it is difficult to tell whether the bottom portion of the crack is real or the artifact caused by FIB. The black arrows in **(d)** point at the faint lateral cracks propagating from the halfway of the median crack.

beneath the impression. Interestingly, the subsurface crack initiated from the faceted pore and passed through the pore on the way of propagation. In addition, a crack free zone can be observed right beneath the center of the impression, suggesting the presence of the residual compression that prevents cracking.

Compared with those in the pure boron carbide, boron-doped boron carbide exhibits a cracking behavior closer to what have been reported for amorphous brittle materials [20]. Still, there is need to justify the repeatability of the observed phenomena in this material.

4.4.3 Boron/Silicon Co-doped Boron Carbide

The serial cross-sections made at selected locations of a 500mN-load impression and the corresponding SEM images are presented in **Figure 4.13**. Similar to the other two materials, the very front portion of the subsurface crack cannot be observed from the surface view. Therefore, in this content, those denotes as the radial crack tip are in fact not the actual crack tip since the very front portion of the radial crack has yet propagated to the surface. A probable method to observe the subsurface view of the radial crack tip is by placing the FIB milling box further away from the tip of its surface trace. And then with successive slicing, the morphology of the radial crack tip could be revealed.

In **Figure 4.13 (c)**, it can be seen that a lateral crack branch out from the radial crack. As previously appeared in the other two materials, the lateral crack does not take place until close to the corner of the impression. The reason behind the phenomenon may stem from the complicated stress field within impression. When the FIB process arrived at the midpoint between the corner and the center of the impression, cracking became more severe and complicated, as shown in **Figure 4.13 (d)**. In addition to the primary subsurface crack as observed in pure boron carbide, there is a crack seemingly initiated from the edge crack at the surface. Eventually, the FIB

process arrived at the center of the impression. Unfortunately, a secondary phase located right beneath the impression, which then alters the expected stress field and results in a different cracking morphology. As appeared in **Figure 4.13 (e)**, a crack initiated form the faceted secondary phase where might act as a stress concentration cite to promote cracking. Despite the unexpected interference, there is still a crack free zone right beneath the center of the impression, signifying the presence of compressive stress field. However, it is out of surprise that the

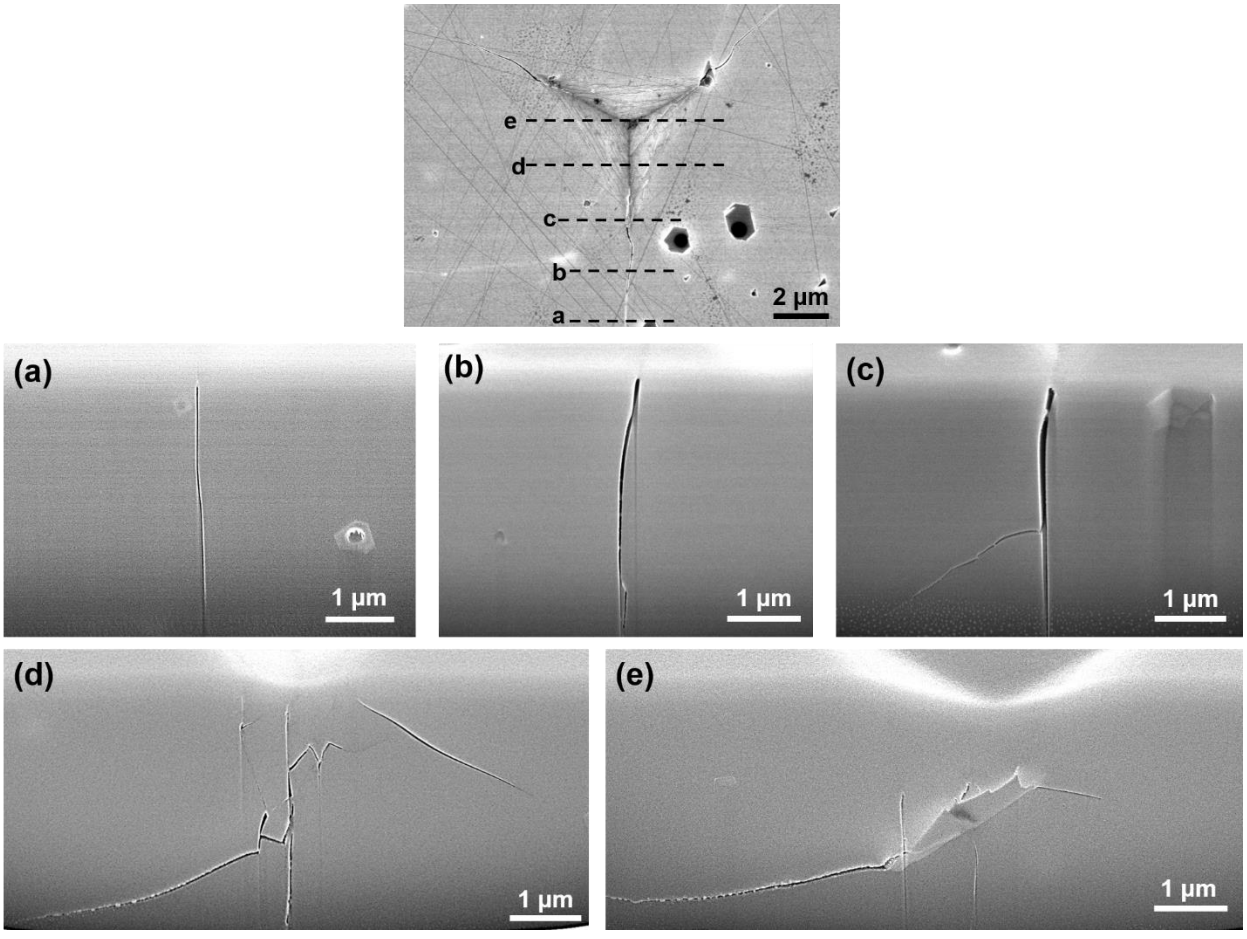

Figure 4.13 An indentation made at a load of 500mN in B/Si co-doped boron carbide. Serial cross-sections made at selected locations indicated in the surface view at the top are shown in **(a)**, **(b)**, **(c)**, **(d)**, and **(e)**. Note that there is a secondary phase right beneath the impression. The black arrow in **(d)** signifies the potential site for the secondary subsurface crack to initiate.

presence of the secondary phase does not largely influence the overall cracking behavior, at least for that outside of the impression.

4.4.4 The Effect of Dopants on Subsurface Cracking Behavior

So far, the dopants have a discernible influence on the cracking behavior at the surface, as presented in **Section 4.3**. The incorporation of dopants into the boron carbide matrix results in longer radial cracks. Unfortunately, in this content it is yet to concluded the influence of dopants on the subsurface cracking behavior since the repeatability of the subsurface morphology has not been verified. Despite of that, here the semi-qualitative results will be used for direct comparison.

For B doping alone, it is surprised to observe that the overall cracking behavior is close to what have been observed for amorphous brittle materials [20], with a median crack straight down rather than off from the centerline. Also, the expected crack tip blunting was not observed throughout the FIB experiments. Therefore, it is believed that the substantial difference in the cracking behavior between pure boron carbide and B-doped boron carbide stems from the mitigation of amorphization in the material, and then the previous postulation on the anomalously higher indentation fracture toughness may not hold true. In **Section 2**, it has been discussed how amorphization affects the mechanical responses in boron carbide, and therefore with the addition of boron dopant, the resultant distorted rhombohedral unit cell could toughen the material by favoring the local plasticity [3]. Eventually, the mechanism manifests itself in shorter surface crack lengths, near-perfect half-penny crack, and higher indentation fracture toughness in B-doped boron carbide.

Now that with Si atoms being doped into the matrix, supposedly the cracking should at least less severe than that in pure boron carbide due to the mitigation of amorphization, as

described for B-doped boron carbide. In fact, the cracking in B/Si co-doped boron carbide is as severe as that in the undoped counterpart. Following the same explanation for the B-doped boron carbide, as the chain center position is replaced with Si atom, there is an extra bond formed between Si and the neighboring icosahedral boron, thus leading to a kinked structure rather than a linear one. This change may no longer favor the local plasticity, and in turn promote the cracking to take place, regardless that Si doping has been reported effective on mitigating amorphization [4, 5, 11]. Another possible explanation to the severe cracking originates from the reduced amount of strong covalent bond in the material due to Si doping. This has been addressed in the previous section where the intrinsic property manifests itself in the lowest hardness value among the three materials studied in this writing.

4.4.5 Summary

In this section, regardless whether the results are representative, the subsurface cracking behavior of the doped and undoped boron carbide has been studied systematically in terms of the influence of dopants. By direct comparison, B-doped boron carbide exhibits a moderate cracking behavior, and a near perfect half-penny crack was observed in this material. The other two materials, on the contrary, developed severe cracking during indentation, whereas the mechanism behind the similar cracking behavior was different for each material, with amorphization triggered in pure boron carbide and the intrinsically weaker bonding nature in B/Si co-doped boron carbide. Despite of that, there is a need to perform another round of experiment to justify the observed cracking behavior presented in this content.

4.5 References

1. Vladislav Domnich, S.R., Richard A. Haber, Manish Chhowalla, *Boron Carbide: Structure, Properties, and Stability under Stress.* Journal of American Ceramic Society, 2011. **94**: p. 3605-3628.

2. Chun Cheng, K.M.R., Akihiko Hirata, Takeshi Fujita, Mingwei Chen, *Structure and mechanical properties of boron-rich boron carbides.* Journal of the European Ceramic Society, 2017. **37**: p. 4514-4523.

3. Kelvin Y. Xie, V.D., Lukasz Farbaniec, Bin Chen, Kanak Kuwelkar, Luoning Ma, James W. McCauley, Richard A. Haber, K.T. Ramesh, Mingwei Chen, Kevin J. Hemker, *Microstructural characterization of boron-rich boron carbide.* Acta Materialia, 2017. **136**: p. 202-214.

4. Sisi Xiang, L.M., Bruce Yang, Yvonne Dieudonne, George M. Pharr, Jing Lu, Digvijay Yadav, Chawon Hwang, Jerry C. LaSalvia, Richard A. Haber, Kevin J. Hemker, Kelvin Y. Xie, *Tuning the Deformation Mechanisms of Boron Carbide via Silicon Doping.* Science Advances, 2019.

5. Atta U. Khan, A.M.E., Xiaokun Yang, Vladislav Domnich, Kelvin Y. Xie, Chawon Hwang, Kristopher D. Behler, Mingwei Chen, Qi An, Jerry C. LaSalvia, Kevin J. Hemker, William A. Goddard III, Richard A. Haber, *Locating Si atoms in Si-doped boron carbide: A route to understand amorphization mitigation mechanism.* Acta Materialia, 2018. **157**: p. 106-113.

6. Jae-il Jang and S.W. M. J. Lance, Ting Y. Tsui, G. M. Pharr *Indentation-induced phase transformations in silicon: influences of load, rate and indenter angle on the transformation behavior.* Acta Materialia, 2005. **53**: p. 1759–1770.

7. V. Trabadelo, S.P., F. Saeidi, M. Parlinska-Wojtan, K. Wasmer, *Nanoindentation deformation and cracking in sapphire.* Ceramics International, 2019. **45**: p. 9835–9845.

8. Satoshi Yoshida, J.M., Ken Wada, Takahiro Fujimura, Akihiro Yamada, Naohiro Soga, *Evaluation of Sinking-In and Cracking Behavior of Soda-Lime Glass under Varying Angle of Trigonal Pyramid Indenter.* Frontiers in Materials, 2016. **3**.

9. Trevor F. Page, W.C.O., Carl J. McHargue, *The deformation behavior of ceramic crystals subjected to very low load (nano)indentations.* Journal of Materials Research, 1992. **7**(2): p. 450-473.

10. Grady, D.E., *Hugoniot equation of state and dynamic strength of boron carbide.* Journal of Applied Physics, 2015. **117**.

11. Qirong Yang, C.H., Christopher J. Marvel, Ankur Chauhan, Vladislav Domnich, Atta U. Khan, Jerry C. LaSalvia, Martin P. Harmer, Kevin J. Hemker, Richard A. Haber, *Fabrication and characterization of arc melted Si/B co-doped boron carbide.* Journal of the European Ceramic Society, 2019. **39**(16): p. 5156-5166.

12. Robert F. Cook, G.M.P., *Direct Observation and Analysis of Indentation Cracking in Glasses and Ceramics.* Journal of American Ceramic Society, 1990. **73**(4): p. 787-817.

13. Payel Maiti, A.E., Manjima Bhattacharya, Pradip Sekhar Das, Jiten Ghosh, Anoop Kumar Mukhopadhyay, *Micro pop-in issues in nanoindentation behaviour of 10 ZTA ceramics.* Ceramics International, 2019. **45**: p. 8204–8215.

14. Satoshi Yoshida, M.K., Akiko Yokota, Shohei Sasaki, Akihiro Yamada, Jun Matsuoka, Naohiro Soga, Charles R. Kurkjian, *Direct observation of indentation deformation and cracking of silicate glasses.* Journal of materials research, 2015. **30**: p. 2291-2299.

15. B. R. Lawn, A.G.E., D. B. Marshall, *Elastic/Plastic Indentation Damage in Ceramics: The Mediad/Radial Crack System.* Journal of the American Ceramic Society, 1980. **63**(9-10): p. 574-581.

16. Jae-il Jang, G.M.P., *Influence of indenter angle on cracking in Si and Ge during nanoindentation.* Acta Materialia, 2008. **56**: p. 4458–4469.

17. Munroe, P.R., *The application of focused ion beam microscopy in the material sciences.* Materials Characterization, 2009. **60**(1): p. 2-13.

18. B. A. Mound, G.M.P., *Nanoindentation of Fused Quartz at Loads Near the Cracking Threshold.* Experimental Mechanics, 2019. **59**(3): p. 369-380.

19. N. Cuadrado, J.S., D. Casellas, M. Anglada, E. Jiménez-Piqué *Geometry of nanoindentation cube-corner cracks observed by FIB tomography: Implication for fracture resistance estimation.* Journal of the European Ceramic Society, 2015. **35**: p. 2949–2955.

20. Mound, B., *Cracking in Fused Quartz During Nanoindentation*, in *Materials Science and Engineering*. 2017, University of Tennessee. p. 165.

5. CONCLUSIONS AND FUTURE WORK

5.1 Conclusions

The objective of this study was to investigate the effect of dopant on the deformation and fracture behavior of boron carbide. This objective is achieved by understanding their nanomechanical responses with advanced testing and characterization techniques, such as nanoindentation, XRD, Raman, SEM, and FIB serial-sectioning. By analyzing results from the aforementioned techniques, the new discoveries are summarized as follows:

1. From the XRD patterns and Raman spectra, the chemical homogeneity was confirmed in all three materials, thus the corresponding mechanical responses are representative to each material.
2. Doping leads to lower elastic modulus and hardness values in boron carbide, primarily because of the reduced amount of strong covalent bond (B-C) present in the systems.
3. The first pop-in events observed in pure boron carbide and B/Si co-doped boron carbide are associated with the onset of plasticity. The corresponding maximum shear stresses were calculated via the power law fitting and standard Hertzian contact fitting to the loading curve prior to the first pop-in event (25.94 ± 0.57 GPa for the undoped boron carbide and 24.47 ± 0.52 GPa for the B/Si co-doped boron carbide). The results approximate the reported shear stresses to initiate amorphization in boron carbide.
4. The load levels to trigger the first pop-in events in the B-doped boron carbide is rather scattered. Thus, the maximum shear stress values could not be derived from the approach described above.

5. Using the modified LEM model, B-doping results in a substantially higher indentation fracture toughness than undoped and B/Si co-doped samples. This is probably due to the resultant crystal structure favoring the local plasticity.
6. From the results of serial FIB cross-sectioning, lateral cracks were observed branching out from the median cracks in the undoped and B/Si co-doped samples as soon as the FIB process approached to the corner of the indentation impression, whereas the B-doped sample displayed a near-perfect half-penny cracking system.
7. The improved tolerance to cracking leads to the observed near-perfect half-penny crack beneath the indentation impression, where the LEM model provides a more accurate indentation fracture toughness estimation.
8. The cracking (both surface and subsurface) in pure boron carbide and B/Si co-doped boron carbide is more severe compared with that of B-doped boron carbide. However, the exact mechanisms governing the similarities and differences in the cracking behavior are not known, which deserves mechanistic modeling effort from our collaborators.

5.2 Future Work

To better understand the nanomechanical responses in boron carbide, especially the cracking behavior, two levels of future work are proposed.

The first level would be completing what have been left due to the COVID-19 pandemic. Once the university re-opens, another round of serial FIB cross-sectioning will be conducted to confirm the repeatability of the observed cracking behaviors in this thesis. Also, nanoindentation tests will be performed again on the B-doped boron carbide to analyze the first pop-in events. Lastly, to maintain consistency in SEM imaging, the *Immersion Mode* on the FEI Helios will be applied to the latter works for better revealing the surface features.

The next level of the future work would be the verification of whether the first pop-in events in these materials are indeed associated with the amorphization. This is because the sudden burst in the loading curve may also be attributed to a rapid crack opening. This would require a systematical analysis of the low-load nanoindentation combined with serial-sectioning microscopy and TEM imaging. Armed with this knowledge, a more complete explanation for the nanomechanical responses of boron carbide could be established.